Fabrication of carbon-based metal-free electrocatalyst for chlor-alkali process

Yihan Wang

Supervisor: Prof. Yuan Chen

Co-supervisor: Dr. Shenlong Zhao

A thesis submitted to fulfil requirements for the degree of

Master of Philosophy

School of Chemical and Biomolecular Engineering

Faculty of Engineering

The University of Sydney

October 2021

Declaration

I certify that the intellectual content of this thesis is the product of my own work and that all the assistance received in preparing this thesis and sources have been acknowledged.

Signature: Yihan Wang

10/18/2021

Acknowledgments

First of all, it is my great honor to participate in the research work as an M.Phil. candidate in USYD. I would like to express my gratitude to my lead supervisor Yuan Chen, who gave me this opportunity to work on a high platform, knowing more excellent researchers and accessing various promising research topics. Also, I sincerely appreciate my supervisor Shenlong Zhao with continuous, patiently, proficiency guidance directing me to electrocatalyst field study, improving my academic writing skills, and developing my problem-solving abilities. This thesis could not have been completed without his successive suggestions and funding support.

Second, I would like to acknowledge my seniors in the lab, who provide technical support for my experiment. I would particularly appreciate Yangyang Liu and Haozhu Wang; thank you for teaching me in equipment operation and helping me encounter many difficulties during the experiment. Thanks to Yuzi Xun, Jingyuan Fei, Zongwen Liu, Victor Lo for guiding and performing the characterizations in my thesis, Yuqi Pan, Yuanyuan Yao, Shuzhen Zhang, Yongchao Yang for providing support and suggestions.

Third, I would like to express my greatest respect to this university, where I spent my four years undergraduate, witnessing the perfect time in my whole life. Also, I greatly appreciate all the management and safety staff in the chemical and biomolecular engineering faculty to provide an efficient and safe environment for finalizing my thesis.

Finally, I would like to thank my parents for their backup supports on my academic study and my friends for their moral support.

Authorship attribution statement

Chapter 3 and Chapter 4 are going to be submitted as a research communication.

Yihan Wang, Yangyang Liu, Zixun Yu, Haozhu Wang, Jinyuan Fei, Victor Lo, Zongwen Liu, Shenlong Zhao*, Yuan Chen* Rich N doped carbon aerogel as an effective metal-free electrocatalyst for chlorine evolution reaction.

Author contributions: Yihan Wang synthesized the catalyst and performed the electrochemical testing, drafted the manuscript. Yangyang Liu, Shenlong Zhao guided the experiment and finalized the manuscript. Haozhu Wang helped with the preparation of the figures. Jingyuan Fei, ZixunYu, Zongwen Liu, and Victor Lo performed the materials characterizations. Yuan Chen provided the lab for performing experiments and helped with the manuscript editing.

In addition to the statements above, in cases where I am not the corresponding author of a published item, permission to include the published material has been granted by the corresponding author.

Signature: Yihan Wang

Oct 2021

As supervisor for the candidature upon which this thesis is based, I can confirm that the authorship attribution statements above are correct.

Signature: Yuan Chen

Oct 2021

Abstract

Chlorine (Cl_2) gas is the most primary chemical precursor in many industrial manufacturing processes. For nearly half a century, the dimensional stable anode composed of RuO_2 and TiO_2 deposited on the Ti substrate has been widely used in the chlor-alkali process. However, the high cost, low product efficiency, and substrate passivation issues severely challenge the further commercialization of Cl_2 production. Along with tremendous effort to reduce the precious metal load and develop non-precious metal to substitute the expensive and scarce Ruthenium-based mixed metal oxides, novel carbon-based electrocatalysts attracts considerable attention. Significant outbreaks have been achieved on metal-carbon hybrid electrocatalysts and demonstrated that carbon materials could be a promising CER candidate.

Herein, we reported a rationally-designed, abundantly N-doped carbon aerogel that could serve as a cost-effective metal-free electrocatalyst for efficiently electrocatalytic chloride oxidation. The electrocatalyst was synthesized through a facile, scalable, and environmental process, including freeze-drying the biomass-derived hydrogel and one-step calcination. The fabricated electrocatalyst exhibited excellent electrochemical performance with 295 mV to achieve 10 mA cm^{-2} and above 95% faradaic efficiency over 30 min, superior to the most transition metal-based electrocatalyst in CER. This work opens up a promising direction in the affordable and efficient chlor-alkali process.

Table of Contents

List of Figures and Tables

List of Abbreviations

Abbreviations	Name
ATO	Antimony-doped tin oxide
BET	Brunauer-Emmett-Teller
CV	Cyclic voltammogram
CER	Chlorine evolution reaction
CE	Carbon electrode
CNT	Carbon nanotube
DSA	Dimensional stable anode
EIS	Electrochemical impedance spectroscopy
ECSA	Electrochemical surface area
FE	Faradaic efficiency
FTO	Fluorine-doped tin oxide
HER	Hydrogen evolution reaction
ICP	Inductively coupled plasma
MMOs	Mixed metal oxides
NCA	N doped carbon aerogel
ORR	Oxygen reduction reaction
RHE	Reversible hydrogen electrode
SHE	Standard hydrogen electrode
SEM	Scanning electron microscopy
SAC	Single atom catalyst
TMO	Transition metal oxide
XRD	X-ray diffraction
XPS	X-ray photoelectron spectroscopy
2D	Two dimensional

Chapter 1. Introduction

1.1 Chlor-alkali process

Chlorine (Cl_2), as the most significant precursors, has been widely used in many chemical industrial processes, for instance, pharmaceutical synthesis, wastewater treatment, and disinfection suppliers and etc.[1] Up till 2020, the world Cl_2 demand has been up to 88 million tons annually, as statistics reported in the World Chlorine Council report.[2] Industrially, the Cl_2 production relies mainly on the chlor-alkali process comprising two important reactions, chlorine evolution reaction (CER) and alkaline production, respectively. Specifically, along with anodic chloride discharged to form Cl_2, the cathodic water simultaneously discharged to form NaOH. The produced Cl_2 could further react with the NaOH to form a series of intermediates such as $HOCl^-$, $ClO^-$and ClO_3^-.[1] Therefore, it is crucial to keep the anodic and cathodic chambers separate from each other. Over the past years, there have been successive breakthroughs in the chlor-alkali process.

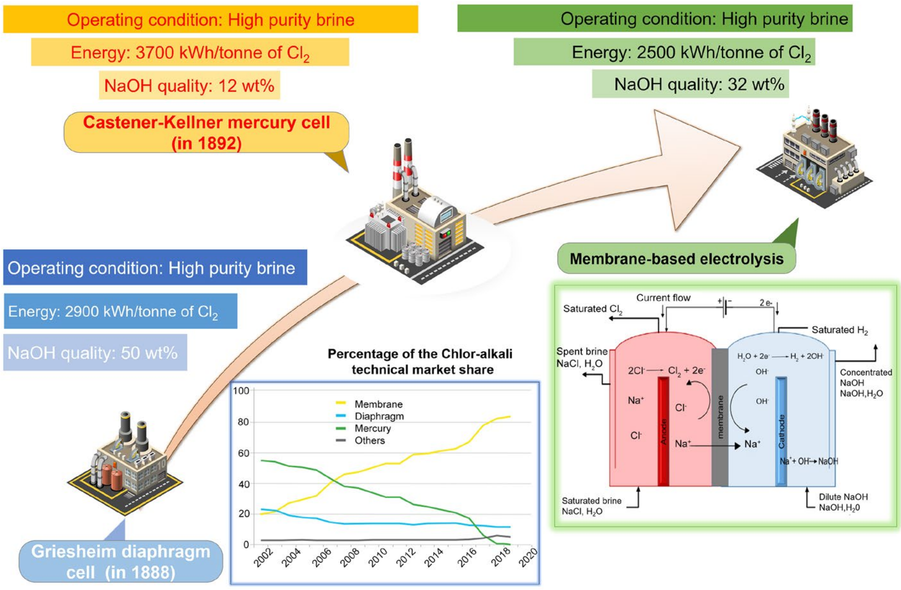

Figure 1. Progress of chlor-alkali process industrial technical development. Reproduced with permission.[3] Copyright 2021, Royal Society of Chemistry.

Industrial technical development primarily prompts the production efficiency in the chlor-alkali process, as shown in Figure 1. The earliest Griesheim diaphragm cell was first constructed in 1888.[4] The capital cost of the overall implementation is low, mainly using the asbestos fibers to separate two compartments. There was a higher level in the anodic chamber; thus, the unreacted NaCl solution would flow into the cathodic chamber, then be discharged with the NaOH. However, the large utilization of the diaphragm cell was limited by environmental issues, as asbestos exposure resulted in an increased risk of lung cancer. The second appeared mercury cell was developed at the same period as the diaphragm cell. The flowing mercury transported the Na^+ from the anode to the cathode and circulated back to sustain the production.[5] The mercury cell process required less concentrated NaCl solution as the feedstock and enabled a large capacity production. However, it is even less environmental than the diaphragm cell owing to a toxic mercury waste included during the process. Since the mercury poisoning (Ontario Minamata disease) occurred in Japan and Canada, industrial mercury cell has been forbidden by most countries.[6] The membrane-based electrolysis was slowly developed until the selective cation exchange membrane employed. Similar to the diaphragm cell, it separates the anodic and cathodic chambers with an eco-friendly membrane instead of asbestos fibers. Among these three techniques, the membrane-based chlor-alkali process with more efficiency and less pollution gained more attention, which has been widely used in industries.[7,8] Up till 2020, the membrane-based chlor-alkali process has shared 85% of the market and has become the predominant industrial Cl_2 production technique.[9]

Another significant outbreak was the anode materials revolution in reducing the energy consumption in the chlor-alkali process. Comparing to the cathodic HER (-0.83 vs. SHE), the anodic CER has a larger energy barrier (1.36 V vs. SHE), determining the overall reaction rate. Therefore, designing out a highly efficient anode is significant in improving performance. The earlier used graphite rod suffered from corrosion under an applied high potential and acidic environment.[10] It was gradually substituted by the noble metal alloys (Pt, Ir) due to their superior stability.[11,12] However, the costly anode materials limited their applicability to small industries. A milestone on the anode development was gained in 1967, the inventor Beer registered the dimensional stable anode (DSA) used in the chlor-alkali process.[13,14] The discovered DSA, containing 30% RuO_2 and 70% TiO_2 coated on a Ti substrate, substantially reduces the overpotential in CER. After that, many attempts have been conducted to further enhance the performance by introducing the other metal oxides described in Chapter 2, Section 2.1. The revolution of the DSA declined nearly 20% of the energy consumption in the chlor-alkali process, which is regarded as one of the most significant electrochemical breakthroughs in the previous 50 years.[15]

The past years witnessed the success of the chlor-alkali process, however, there are some limitations on further improvement of the anode materials. First, the current industrial employed DSA still constitutes a large proportion of the precious metal Ru, imposing high economic pressure. The scarcity of the Ru also challenges sustainable utilization in the future.[16] Second, the DSA, composed of mixed metal oxides (MMOs), suffers from the selectivity issue.[17–20] To be more specific, along with the Cl^- discharged, the oxygen evolution reaction (OER) also occurs in the anode which impact the current efficiency toward Cl_2. Since MMOs possess high activity in OER, their selectivity in CER remains challenging. Therefore, most industries generally concentrate and acidify the electrolyte to enhance the Cl_2 purity.[1] However, this approach brings the third problem, the activity degradation under harsh electrolysing conditions. To be more specific, the susceptible Ru sites dissociation from the catalytic coating leads to inferior catalytic performance, eventually results in a large overpotential.[21] Besides, the Ru-based MMOs coating manufactured by high-temperature pyrolysis will result in “Mud crack” morphologies as Figure 2 b shown.[22] The cracks on the coating, as the penetrating tunnels, enables the acidic electrolyte and oxidizing product accessible to the Ti substrate, and subsequently form a passivation TiO_2 layer, which further accelerate the catalyst degradation.[23]

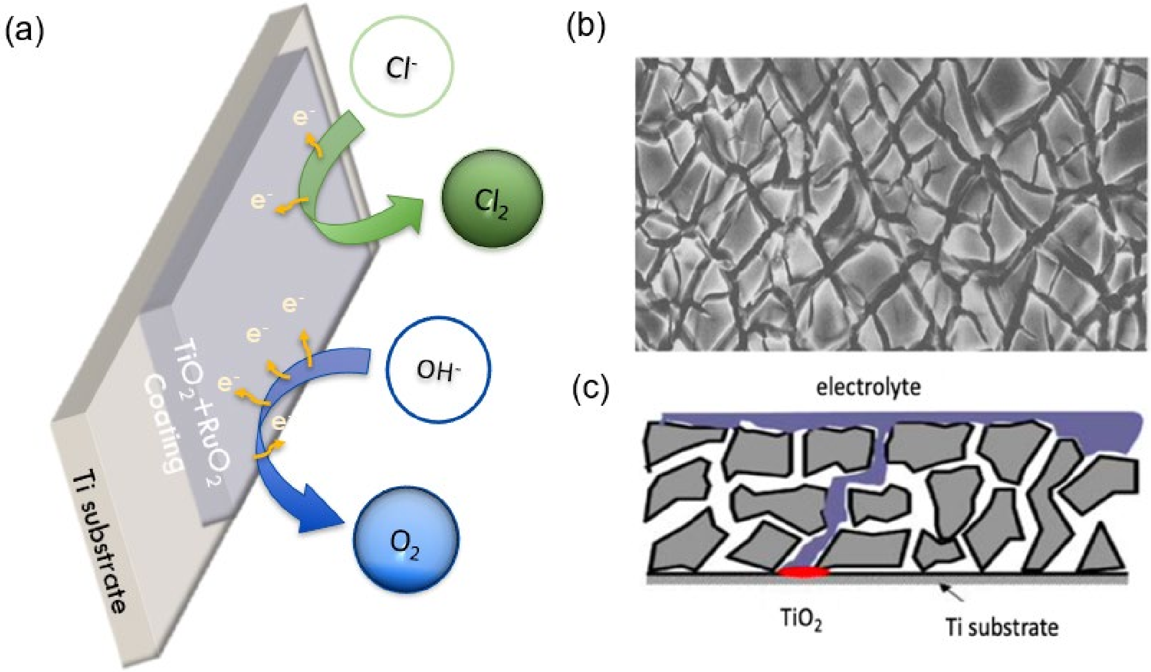

Figure 2. (a) Schematic illustration of the selectivity problem. (b) Mud crack morphology of the DSA.[22] (c) Schematic illustration of the electrolyte penetration. Reproduced with permission. [18] Copyright 2012, De Gruyter.

1.2 Fundamental mechanism of CER

Over the years, much research has been devoted to gaining a deep insight to the competition between OER and CER. As a comparison in Equation (1-2), the OER is more thermodynamically preferred with less standard equilibrium potential. Nevertheless, the CER is more kinetically preferred with merely 2 electrons included process. Thus, the 4 electrons OER could be suppressed by acidifying and concentrating the [Cl^-] in the electrolyte. The industrial chlor-alkali process also accelerates the CER by operating under a high temperature (> 80 °C).

$2Cl^{-} - 2e^{-} \rightarrow Cl_2$ Equilibrium potential: 1.36V SHE (1)

$2H_2O \rightarrow O_2 + 4H^{+} + 4e^{-}$ Equilibrium potential: 1.23V RHE (2)

When underlying the selectivity problem into the atomic scales, the three frequently discussed CER reaction pathways are worth mentioned; that include Volmer-Tafel, Volmer-Heyrovsky, and Krishtalik, as shown below.

Volmer-Tafel (V-T)

$$2\mathrm{Cl}^{-} + 2* \rightarrow 2\mathrm{Cl}* + 2\mathrm{e}^{-}$$

$$\mathrm{Cl}* + \mathrm{Cl}* \rightarrow 2* + \mathrm{Cl}_2$$

Volmer-Heyrovsky (V-H)

$$\mathbf{2Cl^{-} + * \rightarrow Cl * + e^{-} + Cl^{-}}$$

$$\mathbf{Cl * + Cl^{-} \rightarrow * + Cl_2 + e^{-}}$$

Krishtalik

$$\mathbf{2Cl^{-} + * \rightarrow Cl * + e^{-} + Cl^{-}}$$

$$\mathbf{Cl * + Cl^{-} \rightarrow Cl *^{+} + e^{-} + Cl^{-}}$$

$$\mathbf{Cl *^{+} + Cl^{-} \rightarrow * + Cl_2}$$

"*" refers to the active sites.

Among these three mechanisms, the V-H was identified as the most preferable one to explain the high performance on the RuO_2 (110), with less Gibbs energy loss shown on Figure 3 a. Comparing to the Heyrovsky step, the combination of the Cl^{-} in the Volmer step is mostly uphill with 0.13 V energy loss, which could be regarded as the rate determine step.[24] In a deep insight, the rutile RuO_2(110) structure are fully covered with the on-top oxygen (O_{ot}) under the applied potential above 1.36 V *vs.* SHE (Figure 3 b). These O_{ot} are served as the highly efficient active sites (*) to absorb Cl$^-$ and form the intermediate product (ClO_{ot}) in theoretical studies.[19,20,25–28] However, "O_{ot}" sites show a remarkable ability on bonding with OH$^-$ as well, which results in a difficulty in breaking with the current linear scaling relationship between CER and OER (Figure 3 c). This is a mechanistic explanation of the selectivity problem occurring on the most metal oxides.

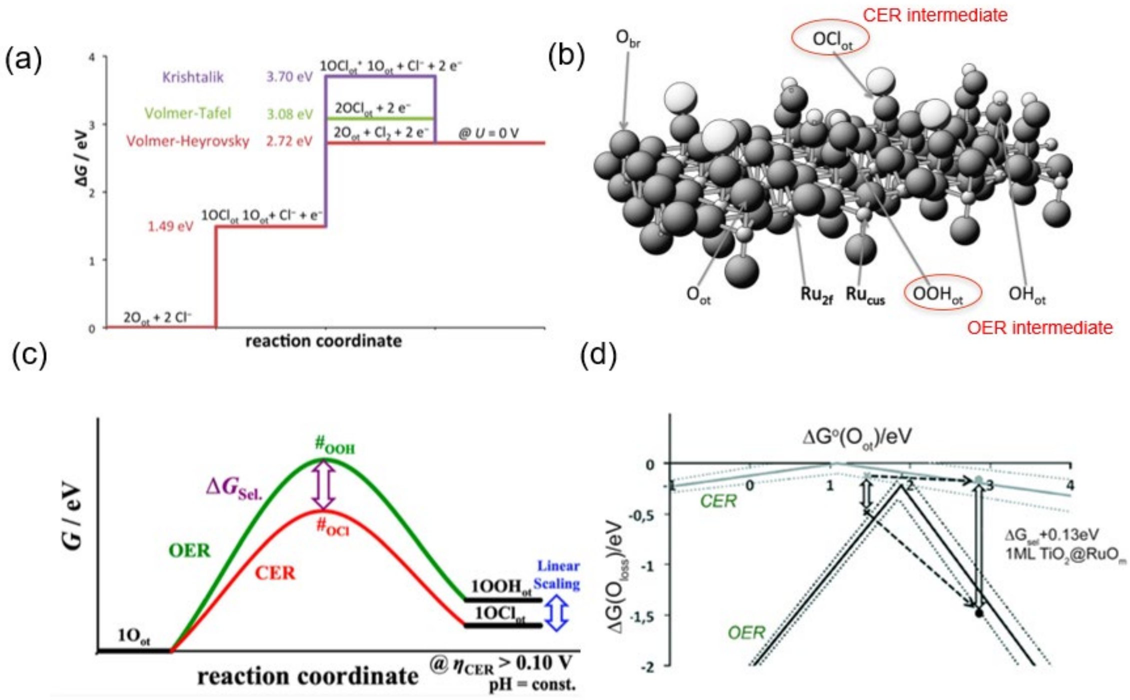

Figure 3. (a) Gibbs free energy of the three proposed CER mechanism pathways at overpotential of 0 eV. Reproduced with permission.[24] Copyright 2014, Springer Nature. (b) Various absorbates on the $RuO_2(110)$ for the CER and OER. O_{br}: under-coordinated bridge sties. O_{ot}: on top oxygen sites. Ru_{2f}: two-fold Ru sites. Ru_{cus}: under-coordinated Ru sites. OCl_{ot}: Cl$^-$ adsorbed on the O_{ot}. OOH_{ot}: OH$^-$ adsorbed on the O_{ot}. OH_{ot}: H$^+$ absorbed on the O_{ot}. Reproduced with permission.[25] Copyright 2014, Wiley-VCH (c) Linear scaling relationship of forming the intermediates OOH_{ot} and OCl_{ot}. ΔG_{sel}: the difference between OOH_{ot} and OCl_{ot}. Reproduced with permission. [20] 2014, Wiley-VCH (d) Volcano plot showing the competition relation between CER (green) and OER (black) occurring on $RuO_2(110)$. Dash line is the standard deviations. Black arrows refer to weaken the Ruo_2 bond by mixing with 1 ML TiO_2. Reproduced with permission. [25] Copyright 2014, Wiley-VCH

Aiming at promoting the selectivity toward CER without sacrificing the activity on RuO_2, Exner et al. first proposed a mechanistic study on replacing the partial RuO_2 with a single layer of other metal oxides (Figure 3 d).[25] Theoretically, weakening the O_{ot} on the surface of the RuO_2 (110) crystalline by 1.5 eV, could efficiently enlarge the gap of energy loss between CER and OER, which results in a more sluggish OER. In fact, the feasibility of this approach has been proven in second-generation DSA, scaling down the RuO_2 composition from 50% to 30% to improve the product efficiency. In 2020, Exner and Lim et al. posed another way to improve the selectivity toward CER by avoiding the intermediate (ClO_{ot}) formation during the process.[29,30] They mentioned that the active sites (*) could be $metal_{cus}$ sites instead of the O_{ot} when atomically dispersed the metal on the carbon substrate, providing a unique platform to absorb the Cl^-.

In recent years, plenty of research has been devoted to exploring the highly efficient electrocatalyst with lower prices and more sustainability. Here, we summarized the recent development of the CER electrocatalyst in the Chapter 2 and proposed an innovative metal-free N doped carbon aerogel that delivers high electrocatalytic ability and well selectivity in Chapter 3 and Chapter 4. We believe that this new work can provide a promising direction in designing a more powerful and economical CER electrocatalyst. Moreover, the chlor-alkali process still holds great potential to be further developed and deeply explored. Finally, we are trying to give some perspectives in Chapter 5 and hope it helps future research.

Chapter 2. Literature Review

This chapter mainly summarized the main advancements in the CER electrocatalyst design. Three sections include, noble metal-based electrocatalyst, transition metal-based electrocatalyst, and carbon hybrid electrocatalyst.

2.1 Noble metal-based electrocatalyst

In spite of the high price, the noble metal-based (Ru, Ir, Pt) electrocatalysts have been long considered as the most powerful electrocatalyst in CER. The preliminary optimizations mainly concentrated on reducing the precious metal loading through mixing with the other earth abundant transition metal oxides (TMO), such as TiO_2, SnO_2, and S_2O_5 or optimizing the geometric structure such as porosity, outstretched surface area, and roughness.

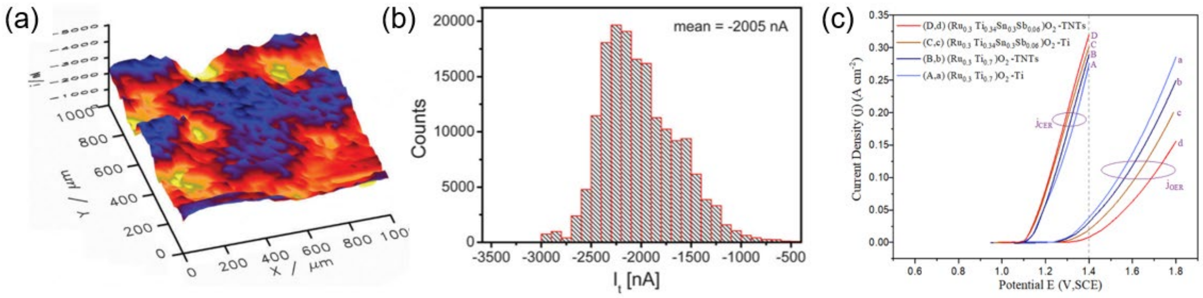

Figure 4. (a) 3D scanning electrochemical microscopy (SECM) of the RuO_2-IrO_2-TiO_2 detected by the controlled current generation and collection tips. (b) Current distribution from the SECM observation. Reproduced with permission.[31] Copyright 2019, Royal Society of Chemistry. (c) Polarization curves of the Sn,Sb co-doped RuTi oxides in 5 M NaCl (CER) and 5M $NaNO_3$ (OER). Reproduced with permission.[32] Copyright 2013, Springer.

The introduction of IrO_2 on the RuO_2-TiO_2 coating was identified as the efficient approach to improve the Cl_2 faradaic efficiency. Schuhmann et al. determined the high selectivity (97%) on the ternary RuO_2-IrO_2-TiO_2 coating through using the differential electrochemical mass spectrometry (DEMS).[31] To gain a deep exploration, the spatial catalytic performance was shown on 3D SECM image and current distribution histogram (Figure 4 a and b). It was investigated that the primary loss of the faradaic efficiency on the ternary RuO_2-IrO_2-TiO_2 was attributed to the local potential variations. The Cl_2 produced on the high active catalytic sites may partially be reduced on the lower catalytic ability sites. Intriguingly, the introduction of the IrO_2 provided a more homogenous surface, which better controlled the local catalytic sites distribution and enhanced the efficiency of Cl_2 production.[33]

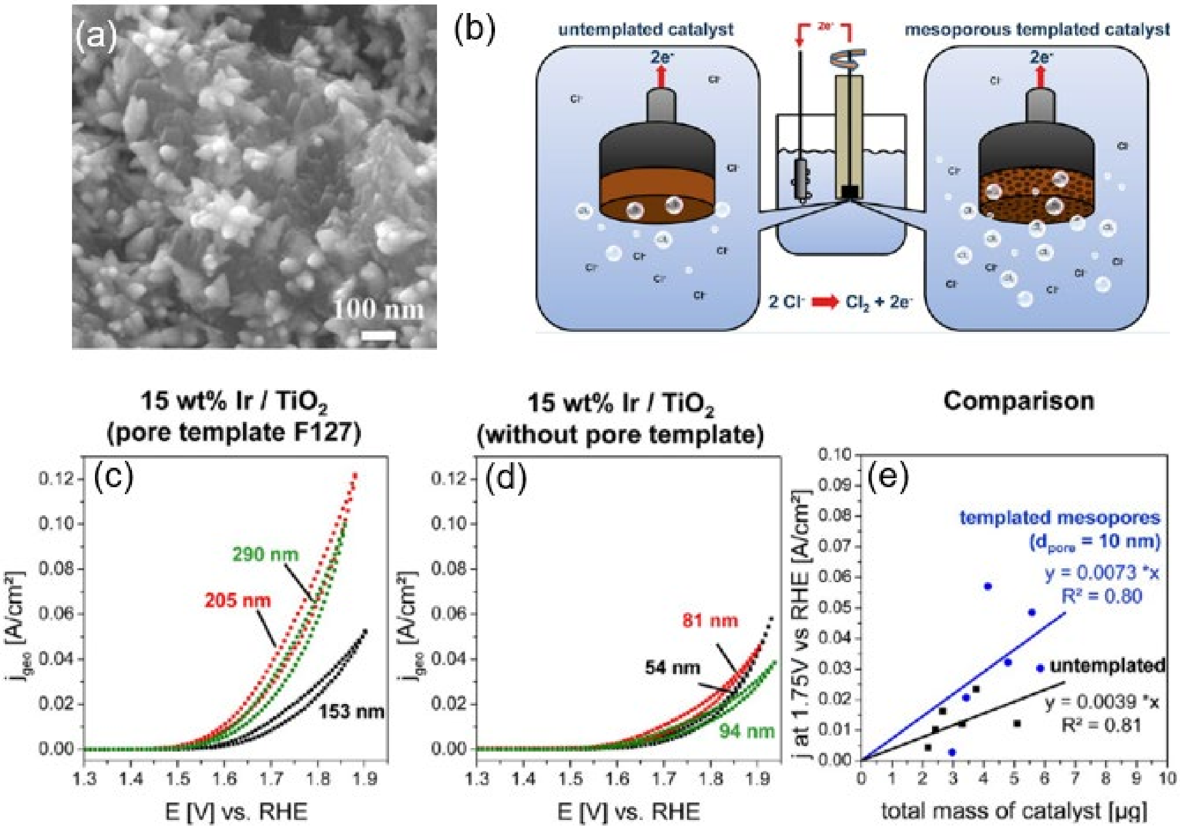

Figure 5. (a) SEM images of the in-situ growth flower-like RuO_2-TiO_2. Reproduced with permission.[34] Copyright 2013, Springer (b) Scheme of untemplated and mesoporous templated catalyst. (c) CV curves for the Ir/TiO_2 with F127 (d) without F127. (e) Current densities generated as a function of the total mass of the templated and untemplated pores catalyst. Reproduced with permission.[35] Copyright 2013, America Chemical Society.

The ternary RuO_2 -SnO_2-S_2O_5 coating has been demonstrated to have a high selectivity toward CER (~90.4%.) as well.[36,37] The fabricated electrode exhibited excellent durability in the seawater electrolysis with estimated five service years under 500 mA cm^{-2} operation. Subsequently, Wei et al. synthesized the RuO_2 -TiO_2-SnO_2-Sb_2O_5 on the TiO_2 nanotube (TNT) through electrochemical anodization.[38] The prepared quandary coating also delivered much higher current density in 5M NaCl than the performance in 5M $NaNO_3$ under an identical condition. Both works demonstrated the SnO_2 and S_2O_5 could optimize the Ru-MMOs selectivity, which holds great potential to be used in future seawater electrolysis.

In addition to mixing with the other components, modifying the microstructure is another effective approach to elevate performance toward CER. The conventional manufacture process of the Ru-MMOs was thermal decomposition, which leads to the severe mud crack morphologies.[39–41] To address this problem, the latter research used the sol-gel method to successfully fabricate the crack-free RuO_2-TiO_2 coating through elaborately controlling the deposition mass loading and drying time. The smooth and homogenous surface obtained by the sol-gel procedure could generate a 10-mA cm^{-2} current density with 50-mV potential, which is less than the conventional thermally decomposed crack-rich electrode.[41] This result revealed that the uniform pore architecture could facilitate bubble removal and accelerate the reaction rate. Besides, the *in situ* growth of the RuO_2 coating on the Ti substrate is found to efficiently avoid the catalyst deactivation brought by mud crack surface morphology.[34] Xiong et al. decorated RuO_2 onto the Ti electrode through a hydrothermal process, and obtained a nanoflower morphology as Figure 5 a shown. It was found that the electrochemical surface area (ECSA) was significantly enlarged (7480 μF cm^{-2}) than the thermally processed RuO_2-TiO_2 electrode coating. Moreover, the *in situ* growth RuO_2-TiO_2 also exhibited good stability without obviously activity recession after 1200 min.

Extensive studies suggested that both the outside surface area and the inside surface are crucial for promoting the gas evolution reaction, especially only two-electrons involved CER which is a fast reaction.[35] Mette et al. fabricated the RuO_2-TiO_2 coating with abundant mesoporous through using the pores template (amphiphilic block-copolymer F127), as shown in Figure 5 b. It was found that the activity of the electrode with mesoporous is nearly 2 times higher than the one without mesopores with the same mass identified by inductively coupled plasma (ICP) (Figure 5 c-d). This work reveals the porosity as a significant parameter in determining the CER performance.

2.2 Transition metal-based electrocatalyst

Even though considerable progress has been made on improving the electrocatalytic performance toward CER mentioned above, the dependence on the precious metal still remains, which is not compatible with the sustainable chlor-alkali economical process. Therefore, earth-abundant transition metals are becoming more attractive in substituting the noble metal constitution in the anode. However, most TMOs exhibit poor electronic conductivity as well as reaction kinetics in the catalytic process, resulting into an inferior performance toward CER.

Over the past decades, some strategies have been employed to optimize the catalytic ability of the TMO-based electrocatalyst in CER. Foreigner doping, as one of the most effective approaches, was recently employed in the quandary MMOs.[42] The transition metal V was used to substitute the Ru in the MMOs. The $Ti_{0.35}$ $V_{0.35}$ $Sn_{0.25}$ $Sb_{0.05}$ oxides coating only required 67 mV overpotential to start the reaction. Bulk mode calculation demonstrated that the V substitution could narrow the bandgaps and facilitate the electron transfer, conducive to the CER.

Other than electronic tunning, structure modification is another efficient approach. For example, Zhu et al. prepared 2D Co_3O_4 nanobelt on fluorine-doped tin oxide (FTO) substrate through hydrothermal synthesis.[43] As the morphologies shown in Figures 6 a and b, the ultrathin nanobelt Co_3O_4 possessed a large surface area, which is conducive to the mass transfer and bubble removal. Most importantly, the nanobelt Co_3O_4 demonstrated a conductivity rivalling to the RuO_2 and a long-term stability for 10 hr in harsh CER conditions, with only 2% current attenuation. Similar but independent research investigated that the transition metal based antimonates $CoSb_2O_5$ on the antimony-doped tin oxide (ATO) substrate was more durable than the commercial $RuTiO_x$ in acidic condition (Figure 6 c and d), with no obviously recession longer than 250 hr under 100 mA cm^{-2}.[44] Intriguingly, both works revealed the outstanding activity as well as stability of the TMOs in CER, especially Co-containing electrocatalysts. However, there is lack of mechanism explorations on TMOs in chloride oxidation.

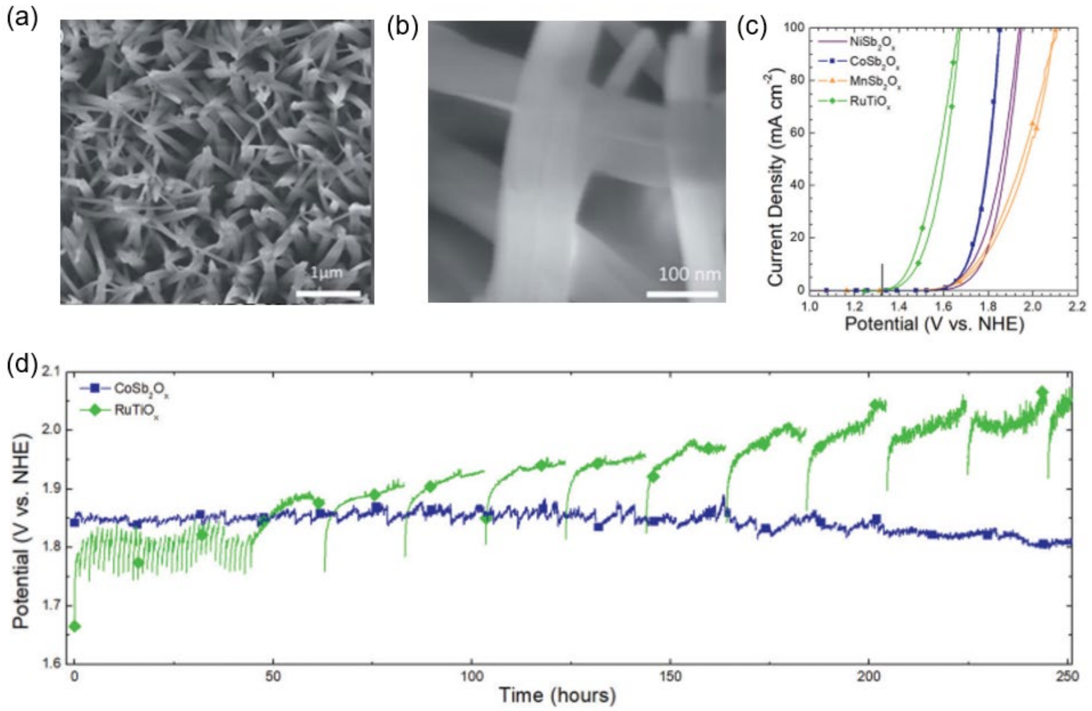

Figure 6. (a) and (b) SEM images of the nanobelt-like Co_3O_4 on FTO. Reproduced with permission.[45] Copyright 2018, Royal Society of Chemistry. (c) Cyclic voltammetry electrochemical testing of the

Ni, Mn, Co antimonates on ATO. (d) Chronopotentiometry testing of $CoSb_2O_5$ during 250 hr. Reproduced with permission.[44] Copyright 2019, Royal Society of Chemistry.

2.3 Carbon hybrid electrocatalyst

The carbon materials, owing to their low cost, superior conductivity as well as large surface area, attract numerous interest in promoting the electrocatalytic performance through a metal-substrate interaction in various reaction.[42,46] Recently, some research works have revealed metal-incorporated carbon-supported electrocatalysts' high performance in CER.[47–49]

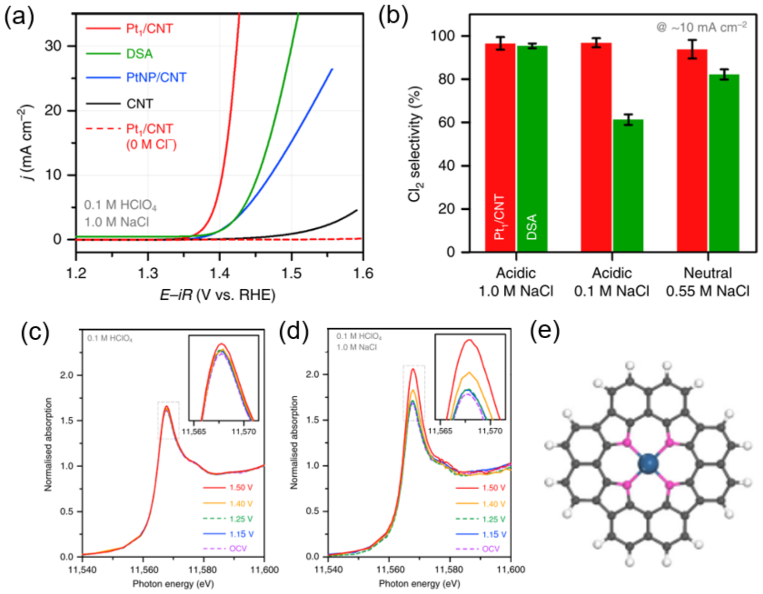

Figure 7. (a) LSV curves of Pt/CNT and PtNP/CNT and commercial DSA. (b) Cl_2 Selectivity of Pt/CNT and commercial DSA in different electrolyte conditions. (c) Pt L3-edge XANES spectra of the Pt/CNT in Cl^- absent electrolyte and (d) Cl^- present electrolyte. (e) Schematic drawing of the Pt-N_4C_{12} (blue ball: Platinum, pink ball: nitrogen, grey ball: carbon, white ball: hydrogen). Reproduced with permission.[45] Copyright 2020, Springer Nature.

Lim et al. synthesised atomically dispersed Pt sites on the carbon nanotube (Pt/CNT) through heat pyrolyzing a Pt porphyrin precursor.[45] The as-synthesised CER electrocatalyst exhibited superior activity as well as the selectivity than the nanoparticle dispersed sites (Pt-NP/CNT) and commercial DSA as shown in Figure 7 (a-b). Through observing in-situ XANES spectrums, there was an apparent upward move in Cl^- contained electrolyte, particularly above 1.40 V where the CER most possible occurs. However, there was negligible change occurring in Cl^- absent electrolyte. The difference reveals that the Cl^- possibly absorbed on the Pt sites under the applied potential for CER, which could explain the high selectivity ability may originate from single-atom Pt active sites (Figure 7 c-d). Through deep mechanism exploration, it was found that $Pt\text{-}N_4C_{12}$ is the most preferable structure for CER, as Figure 7 (e). The author inferred that the exceptional selectivity was attributed to the Cl^- was directly absorbed on the $Pt\text{-}N_4C_{12}$ sites rather than O_{cus} sites, which could efficiently break down the intimately relationship between OER and CER.[29,30] This study paved a promising avenue to hinder the parasitic side of OER through incorporating carbon materials as a substrate.

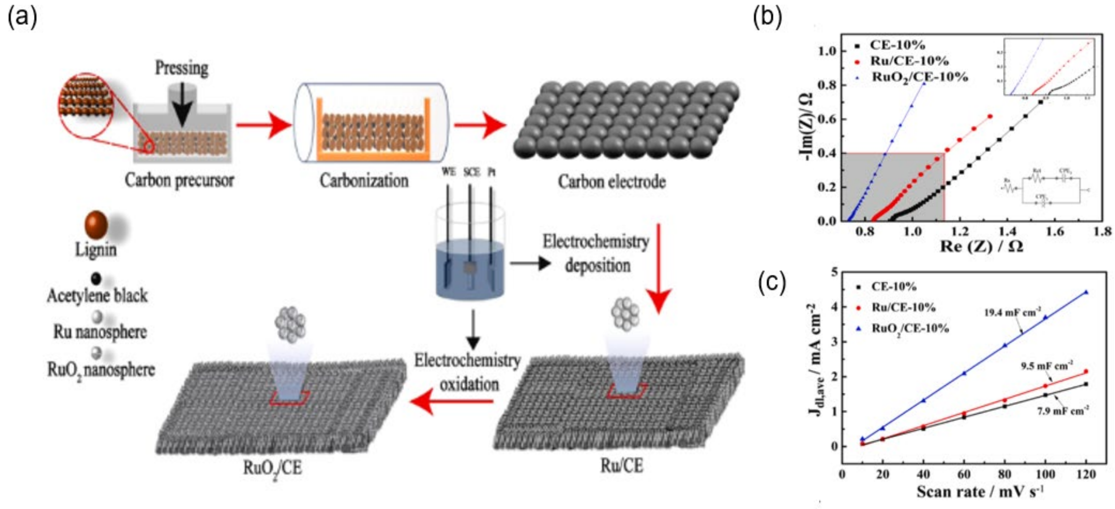

Figure 8. (a) Schematic illustration of Ru doped carbon electrode fabrication process. (b) EIS results comparison and (c) Double layer capacitance comparison of the carbon electrode, Ru doped carbon

electrode with 10% carbon black and without. Reproduced with permission.[50] Copyright 2021, Elsevier.

Recently, Chi et al. has fabricated a RuO_2 doped biomass-derived carbon electrode through high temperature pyrolyzing of the lignin and acetylene black mixture, followed by electrodeposition and carbonization, as shown in Figure 8 (a).[50] Compared with the conventional Ti substrate, the carbon substrate could well-eliminate the Ti substrate passivation issue caused by mud cracks on MMOs. Additionally, it was also found that the narrow irregular pores on the hierarchical interconnected structure could form with an optimal 10% acetylene black addition on the carbon electrode. The RuO_2 doped carbon electrode also demonstrates excellent conductivity as well as large ECSA, as shown in Figure 8 (b-c). The porous carbon electrode also delivered a more stable performance with over 3000 s lifetime, which was better than the compact graphite electrode with only a 1500 s lifetime under an identical condition.

Both above works illustrated the carbon materials could play as promising candidatures on CER electrocatalyst design. Considering with the harsh electrolyte conditions in CER, the carbon substrate outperforms the conventional Ti substrate with better elimination of passivation issue and "ClO_{ot}" intermediate formation. [29,30] Moreover, carbon materials could be processed and modified easily through ball milling, chemical vapor deposition, sol-gel, and high-temperature pyrolysis, etc. [51] Most significantly, the carbon materials are advantageous of cost-effectiveness, plentifully resource, and environment friendness.[52] To sum up, the metal-free carbon-based electrocatalyst holds a great potential to utilize on the current noble metal-based chlor-alkali process. However, pristine carbon still shows the limitation, such as poor instinct properties for the catalytic process. There are a plenty of efficient strategies, such as doping heteroatoms, creating defects, and improving structure porosity, developed to optimize the carbon-based electrocatalyst, especially in oxygen reduction reaction (ORR) and energy storage.[46,48] Although the advancement of the metal-free electrocatalyst has attracted significant attention, employment in the CER field has not been considered so far. Therefore, it holds tremendous potential in utilizing metal-free materials in substituting the conventional noble metal oxide-based electrode for the chlor-alkali process.

Chapter 3. Experiment Setup and Characterization

Chemicals: Materials specifications used in the experiment are indicated as follows.

Commercial ι-carrageenan, urea (99%-100.5%), sodium chloride (NaCl, ≥ 99%), sodium nitrate ($NaNO_3$, ≥ 99%), sodium perchlorate ($NaClO_4$ ≥ 98%), perchloric acid ($HClO_4$, 70%), soluble starch powder (ACS, for indicator), sodium thiosulfate ($Na_2S_2O_3$, 99%), potassium iodide (KI, 99%) hydrochloric acid (HCl, 37%), acetone (99.7%), ethanol (94.5%), and Nafion 117 solution (5 wt%) were purchased from Sigma-Aldrich. The carbon cloth (CC) was purchased from Toray Industries Inc. Commercial natural graphite was purchased from Targray Technology International Inc. Argon (Ar, Ultra High Purity Grade G2 Size) was supplied by BOC Australia. All the water used in the experiments is ultrapure deionized water (18.2 MΩ·cm resistivity) acquired via the Thermo Scientific Barnstead Nanopure water purification system.

Synthesis of N doped carrageen-derived carbon aerogel （NCA）: All the N-doped carbon aerogel with different calcinating temperatures is fabricated according to a published procedure.[53] as following.

Typically, the 1 g urea was dissolved in 50 mL DI water at 80 ºC to obtain a clear urea solution (2 wt%), and then 1 g ι-carrageenan powder was added under stirring. The urea-carrageenan solution was kept stirring and heating under 85 ºC for 2 hr to obtain a pale-yellow gel solution. After cooling to room temperature, the urea-carrageenan hydrogel was formed and followed by freezing with liquid nitrogen. The frozen hydrogel was transferred to the freeze dryer for two days to dehydrate and produce urea-carrageenan aerogel. To prepare carrageen-derived carbon aerogel (CA), the pure DI water was heated to 80 ºC and 1 g ι-carrageenan powder was directly added with vigorously stirring. The rest procedures were the same as the fabrication of the NCA abovementioned.

The obtained urea-carrageenan aerogel was then annealed at the desired temperature (500 ºC, 600 ºC, 700 ºC, 800 ºC) at a heating rate of 5 ºC min^{-1} under Ar atmosphere for 1 hr. The resultant carbonized aerogels, which are denoted as NCA-X (X = calcinating temperature), were washed by immersion into the 1 M HCl solution for 24 hr to completely remove the Ca^{2+} and K^{+} impurities and leave the small-sized mesopores on the hierarchical carbon aerogel. The acid-washed NCA-X was also washed by the DI water and dried in a vacuum oven at 60 ºC overnight.

Analytic characterization

All the as-obtained materials characterization was performed as the process shown below.

The morphology images were obtained using a high-resolution scanning electron microscope (HR-SEM, UltraPlus, Zeiss). The geometric surface area and corresponding pore structure were obtained using N_2 physisorption (Autosorb-iQ, Quantachrome). The specific surface area was estimated by using Brunauer-Emmett- Teller (BET) method, ranging from 0.05 and 0.25 (relative pressure P/P_0). The pore size distribution was derived by using the density functional theory (DFT) model. The chemical states and the binding configuration were examined through X-ray photoelectron spectroscopy (XPS, K-Alpha+, Thermo-Fisher Scientific) equipped with an Al-Kα source (1486.8 eV). Spectra was analysed with the aid of Avantange Version 9.0.0.7 software package. Raman spectra results were recorded on Raman microscope (inVia, Renishaw, 532 nm laser excitation).

Electrode preparation: The working electrode wa prepared by depositing the electrocatalyst ink on the CC sheet.

The CC sheet, which was trimmed into 1 x 1 cm^2, was immersed ultrasonically into the acetone, ethanol, and DI water for 30 minutes respectively.[50] Then, the cleaned CC sheet was stored in the vacuum dryer at 60 ºC. To prepare the electrocatalyst inks, 3.7 mg samples were dispersed into a mixed solution, which contains 250 µL DI water, 250 µL ethanol, and 25 µL Nafion (5 wt%), and ultrasonicated for 40 minutes to obtain a homogeneity catalyst ink without any precipitation. Then 10 µL of the ink was deposited and air-dried until the thin film formed on the CC sheet, and the deposition was repeated for the other 4 times. The mass loading on the resultant working electrode is 0.35 mg cm $^{-2}$.

Electrochemical cell construction: All the electrochemical characterizations were performed in a set up two-chamber H-Cell as Figure 9 shown.

The electrolyte was prepared by dropwise dilute 70% $HClO_4$ into the 4 M NaCl solution until the pH values were adjusted to 2 ± 0.05.[44]. The measurement of pH values in the experiment electrolyte were conducted by using a digital pH value meter (LAQUA F-72A-S). The first compartment (left chamber) of the H-cell, which held a counter electrode in 100 mL electrolyte solution, was separated by a cation-selective exchange membrane (Nafion 115 membrane, Dupont) from the second compartment which had the working electrode and reference electrode in another 100 mL electrolyte.

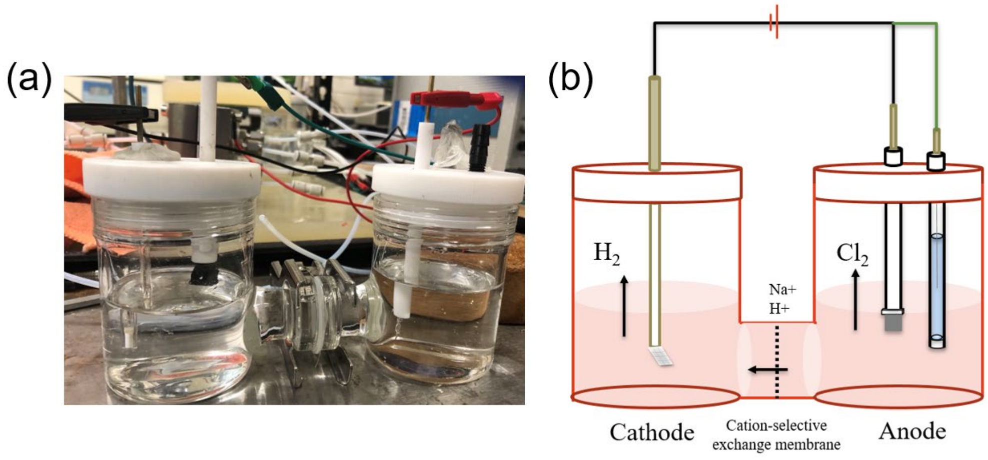

Figure 9. (a) Three-electrode reactor set up in a H-type cell set up. (b) Scheme of the three-electrode configuration. Black line: wires connected to the electric wires. Green lines: wire connected to the reference electrode.

General electrochemical methods. All the electrochemical characterizations were conducted on the electrochemical workstations (CHI 760E, CH instruments). The cyclic voltammogram (CV) was performed at a 500 mV/s scan rate and for more than 50 cycles before the linear sweep voltammetry (LSV) measurement to get a reproducible i-E relationship.[45] All the potentials recorded were converted into reversible hydrogen electrode (RHE) scale using Equation 1. The reference electrode was calibrated through a two-electrode cell, which the Pt wires are the counter electrode. The open-circuit potential (OCP) was measured with continuous purged H_2 gas to obtain the potential under a stable state, the RHE was calibrated with a conversion of the potential between H+/H_2 equilibrium and the reference electrode. All the potentials obtained from the experiment were converted to the RHE according to Equation 1.

$$E_{RHE} = E_{Ag/AgCl} + 0.0591 * pH + 0.197 \qquad \text{Equation 1}$$

The LSV was measured under an Ar purging environment at a scan rate of 10 mV/s with 90% iR compensation. The overpotential was calculated with a subtraction of the Cl^-/Cl_2 equilibrium potential as following Equation 2. The electrolyte environment (pH, Cl^- concentration, partial pressure of the Cl_2) and reaction temperature were considered in the Nernst equation (Equation 3).

$$\eta = E_{CER}\ vs.RHE - E^{o}_{CER} \qquad \text{Equation 2}$$

$$E_{CER}\big((T, a(Cl_2), a(Cl^-)\big)\ vs.RHE = E^{o}_{CER} - \frac{RT}{F} \times lna(Cl^-) + \frac{RT}{2F} \times lna(Cl_2)$$

Equation 3

η: overpotential

E^{o}_{CER}: equilibrium potential

R: gas constant = 8.314 $J{\cdot}K^{-1}{\cdot}mol^{-1}$

F: Faraday constant = 96,485 C/mol

a (Cl^-) = concentration of Cl^- in the electrolyte

a (Cl_2) = partial pressure of Cl_2 in the electrolyte (assume to be 0.01 under Ar purging environment)

The Tafel plot was estimated based on the linear portion of the overpotential and logarithm of the current density as equation 4. The slope of the linear relationship was the Tafel plot, and the exchange current density (j_0) was obtained when the $\eta = 0$. The smallest slope (b) obtained from the function was used for catalyst reaction kinetics comparison. [54]

$$\eta = a + b\ logj \qquad \text{Equation 4}$$

The electrochemical impedance spectroscopy (EIS) measurement was carried out in an Ar-saturated electrolyte under a fixed supplied potential at an overpotential of 295 mV. The employed a 5 mV amplitude of the sinusoidal wave with the frequency ranging from 100,000 Hz to 0.1 Hz. The measurements were performed until the stable Nyquist plots results could be repeatable at least three times. Electrochemical surface area (ECSA) was determined according to Equation 5. The double-layer capacitance (C_{DL}) was estimated by using scan rate-dependent CV measurements within a potential window between 0.92 V and 1.02 V *vs.* RHE (non-faradaic region). The potential scanned in a positive direction, then backward to the most negative potential, was recorded at different scan rates of 5 mV s^{-1}, 10 mV s^{-1}, 30 mV s^{-1}, 50 mV s^{-1}, 100 mV s^{-1}. Before starting the next scan rate measurement, the working electrode was set a quiet time of 10 s to diminish the last sweep impact.

$$ECSA = \frac{C_{DL}}{C_s} \qquad \text{Equation 5}$$

It is assumed that all the current generated in this potential region is originated from the double-layer charging. The middle point current density (i_c) was obtained from calculating the half distance of the current generated at 0.97 V vs. RHE. The linear regression between all the i_c and different scan rates was simulated with a slope equal to the C_{DL}. The Cs is the specific capacitance, which is roughly 0.015-0.110 mF cm^{-2} in acidic electrolytes.[55] Herein, the 0.06 mF cm^{-2} was adopted for the CER occurring in the carbon-based samples.[50]

The faradic efficiency or Cl_2 selectivity was examined using iodometric titration, according to the method from Koper et al.[56]. The Cl_2 selectivity was determined based on the theoretical Cl_2 production yield and experimental Cl_2 production yield, as following Equation 6 shown.

$$Cl_2\ selectivity\ (\%) = 100\ \times \frac{Experimental\ yield}{Theoretical\ yield} \qquad \text{Equation 6}$$

The anode compartment of the H-cell was sealed and filled with 50 mL electrolyte. Before the faradic efficiency measurement, the Ar gas was sparged into the electrolyte for 20 min to reduce the dissolved oxygen content. Chronopotentiometry was then performed under a constant applied potential that could maintain a stable current density well above 10 mA cm^{-2}, lasting for 5 min, 10 min, 30 min, respectively. The theoretical production yield of the Cl_2 was estimated according to the following Equation 7.

$$Theoretical\ yield = \int \frac{i}{2F} dt \qquad \text{Equation 7}$$

i = current

F = Faraday constant = 96,485 C/mol

t = chronopotentiometry measurement time

The experimental production yield of the Cl_2 was estimated by iodometric titration, based on Equations 8 and 9. The electrolyte (10 mL) was immediately transferred into a via, containing the NaI in large access (around 100 times), which could suppress the equilibrium of volatile I_2 formation. After transferring, the electrolyte turns yellow-brown (light yellow for 5 min, dark yellow for 10 min) after steady stand for 2 min, generating I_2 to substitute all the Cl_2 produced from chronopotentiometry measurement. Then, the I_2 in the via was titrated with the standardized 0.01 N $Na_2S_2O_3$ solution until the color changed from yellow-brown to pale yellow. The starch (200 μL, 2 μg) was added, turning the color to the blue in the via, indicating the remaining amount of I_2 presence. Subsequently, the additional 0.01 N $Na_2S_2O_3$ solution was added to finalize the iodometric titration process, and the total volume of that was recorded to estimate the experimental Cl_2 production yield as following Equation 10. All the titration measurements were performed triple times to obtain an average volume.

$$Cl_2 + 2NaI \leftrightarrow I_2 + 2NaCl \qquad \text{Equation 8}$$

$$I_2 + 2Na_2S_2O_3 \leftrightarrow 2NaI + Na_2S_4O_6 \qquad \text{Equation 9}$$

$$Experimental\ yield = \frac{0.01\ N \times V(\mathrm{N}a_2S_2O_3)}{2} \qquad \text{Equation 10}$$

0.01 N = molar concentration of $Na_2S_2O_3$ solution

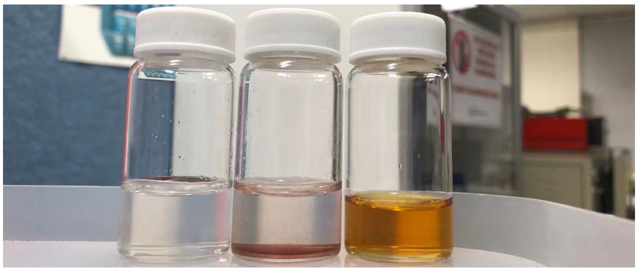

Figure 10. Iodometric titration process (right to left: via containing electrolyte after 30 min reaction, via containing electrolyte after adding $Na_2S_2O_3$, via containing electrolyte after complete titration).

50 μL catalyst ink was deposited on the 1 x 1 cm-2 carbon cloth as a working electrode for the catalyst stability measurement. The H-cell was set up and placed in a temperature-controlled water bath to maintain a uniform thermal environment (25 °C) under a constant applied potential for 24 hr. The LSV measurement was immediately performed after the stability test as a comparison for the catalytic activity degradation.

Chapter 4. Metal-free electrocatalyst for chlorine evolution reaction

This content of the chapter is going to submit as research communication.

Yihan Wang, Yangyang Liu, Zixun Yu, Haozhu Wang, Jinyuan Fei, Victor Lo, Zongwen Liu, Shenlong Zhao*, Yuan Chen* Rich N doped carbon aerogel as an effective metal-free electrocatalyst for chlorine evolution reaction.

Author contributions: Yihan Wang synthesized the catalyst and performed the electrochemical testing, drafted the manuscript. Yangyang Liu, Shenlong Zhao guided the experiment and finalized the manuscript. Haozhu Wang helped with the preparation of the figures. Jingyuan Fei, ZixunYu, Zongwen Liu, and Victor Lo performed the materials characterizations. Yuan Chen provided the lab for conducting experiments and helped with the manuscript editing.

Supervisor name: (Yuan Chen)

4.1 Introduction

Chlorine, as one of the most crucial chemical precursors, is widely required in different critical industrial processes, such as polymer synthesis, wastewater treatment, pharmaceutical, and disinfection commercial good production.[1] The continuously rising demand for the Cl_2 has achieved nearly 88 million tons per year.[2] Currently, the general Cl_2 was produced by a couple of redox reactions, hydrogen evolution reaction (HER) in the cathode and chlorine evolution reaction (CER) in the anode. The CER, which required a comparatively high energy barrier (1.36 V *vs.* SHE), determines the reaction rate of the whole chlor-alkali process. Over the past 50 years, the Ru-based mixed metal oxides (Ru-MMOs), such as dimensional stable anode (DSA), played a dominant role in the industrial CER due to their high efficiency, good conductivity, and well stability.[14] However, the further improvement is hampered by the scarcity and affordability of the large percentages of the precious metal composition.[18] Besides, the Ru-MMOs were identified as a highly efficient OER catalyst in the water splitting, which suggests the intimately coupled relationship between OER and CER during the electrolysis.[25] The product efficiency toward Cl_2 is susceptible impaired by the concomitant water oxidation. Therefore, developing the readily available, abundant, and efficient electrocatalyst still remains challenging.

As one of the most promising materials, metal-free carbon materials have been widely explored due to their excellent conductivity, easy modification process, and abundant earth reserves.[57] Recent studies revealed that the carbon substrate could play a promising role in CER. Lim et al. doped atomically dispersed Pt-N_4 sites on the carbon nanotube (Pt-N_4/CNT).[45] Impressively, the Pt-N_4/CNT exhibited extraordinary selectivity toward CER even in the low Cl^- concentration or neutral environment. Chi et al. fabricated lignin-based carbon electrodes (CE) to substitute conventional Ti substrate.[50] The decorated RuO_2 on CE possessed excellent catalytic activity with significantly reduced conductivity and increased active surface area. Although some outbreaks have been made on metal-based carbon-supported electrocatalyst, metal-free electrocatalyst has not been studied in CER.

The earlier graphite electrode has been once used in industrial, however, the high overpotential significantly challenges its durability.[10] As tremendous progress has been made on enhancing the carbon materials performance in gas evolution reaction, their utilization in CER holds great potential. Since Dai et al. firstly reported the N-doped CNT possessed exceptional catalytic ability in oxygen reduction reaction (ORR), numerous researches are devoted to doping the heteroatoms (N, S, B, P, S) on carbon materials in various electrocatalytic reactions.[58] It was found that the introduction of the heteroatoms could modulate the electronic properties, then tunning the chemical activities.[46–48,51,52,57] In particular, the N, the nearest element to the carbon in the periodic table, possesses a similar atomic size while different electronic configuration. Therefore, the N-doping is comparatively easy with less interruption to the carbon lattice, simultaneously effectively resulting in local charge redistribution with more electronegativity electronic property.[57]

Herein, we report biomass carrageenan-derived carbon aerogel with rich N atom% (11.73%), hierarchical interconnected pore structure, using a facile, convenient, environmental method as an efficient and cost-effective metal-free electrocatalyst for CER. The N was in-situ doped into the carbon matrix with mixing with the N-rich precursor, followed by freeze-drying and one-step calcination among different temperatures. The optimal electrocatalyst exhibits excellent activity (295 mV to generate 10 mV cm^{-2} current density) and CER selectivity (~ 95%) in a harsh environment (4M NaCl, pH =2), even outperform most of the transition metal-based CER electrocatalyst. To the best of our knowledge, this is the first communication discussing metal-free electrocatalyst performance. We hope it could open up an innovative avenue for the future CER electrocatalyst design.

4.2 Results and Discussion

Carrageenan molecules are the high carbon content biomass with the sulfate groups naturally located on the chain structure. As Figure 11 scheme shown, when heating over 80 °C, the rearranged macromolecular chains provided more edge sites in their nanostructures, entrapping the N-rich urea flexibly. The gelation was induced to fully dissolve carrageenan molecules after cooling to room temperature, leaving an aqueous embedded porous structure. With the aid of cations (K^+, Ca^{2+}), derived from the algae extract, the electronic repulsion was suppressed between two monomolecular chains, promoting the better gel formation.[59]

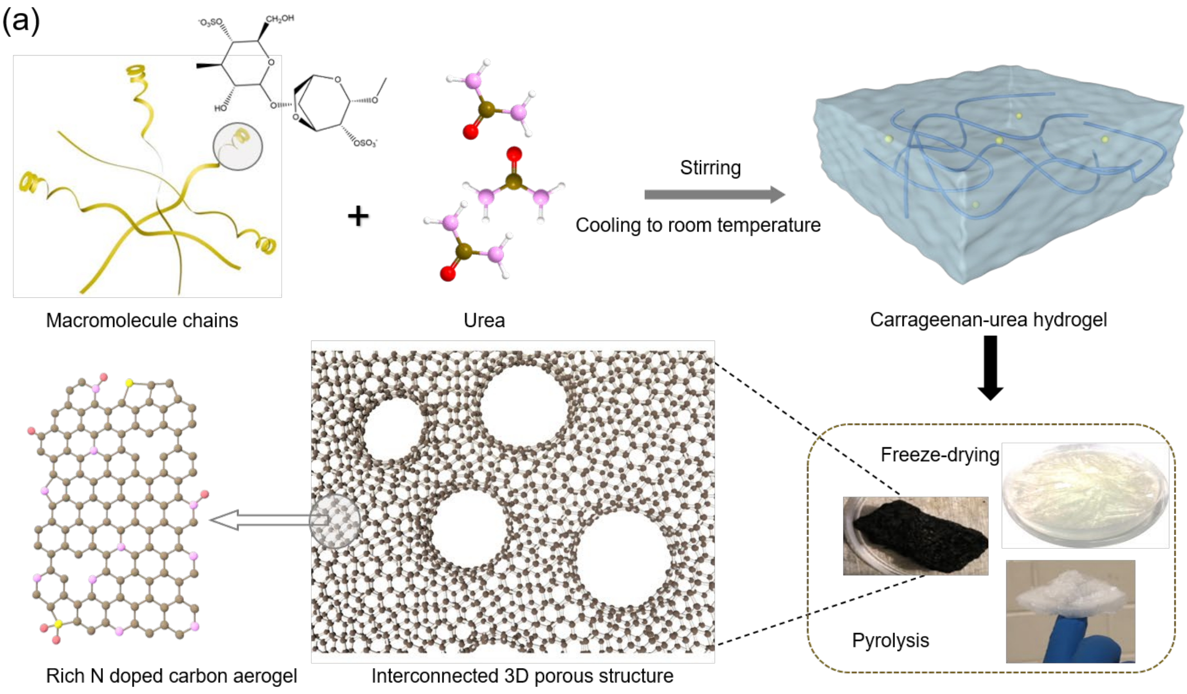

Figure 11. (a) Schematic illustration of the N-doped aerogel fabrication process.

Then, water in a fabricated hydrogel was sublimated by a freeze dryer, and the resultant aerogel was pyrolysis at different temperatures. Among these, the NCA-700 exhibits impressive performance with the best CER activity and selectivity. As can be observed in Figure 12 (a) – (c), the resultant NCA calcinated at 700 °C (NCA-700 °C) possess well sponge-like interconnected porous structure. The macro- and meso- pores distributed on the carbon matrix develop more tunnels for the mass transfer and bubble release, compared to the graphite's compact morphology (Figure S1 a and b). The carbon aerogel without N was characterized by smaller and irregular pores, presenting poor gel formation (Figure S1 c-f). According to the Gartstein et al. reported, the urea could assist in the macromolecular hydrolysis in the aqueous solution, which is conducive to the gelation process.[60]

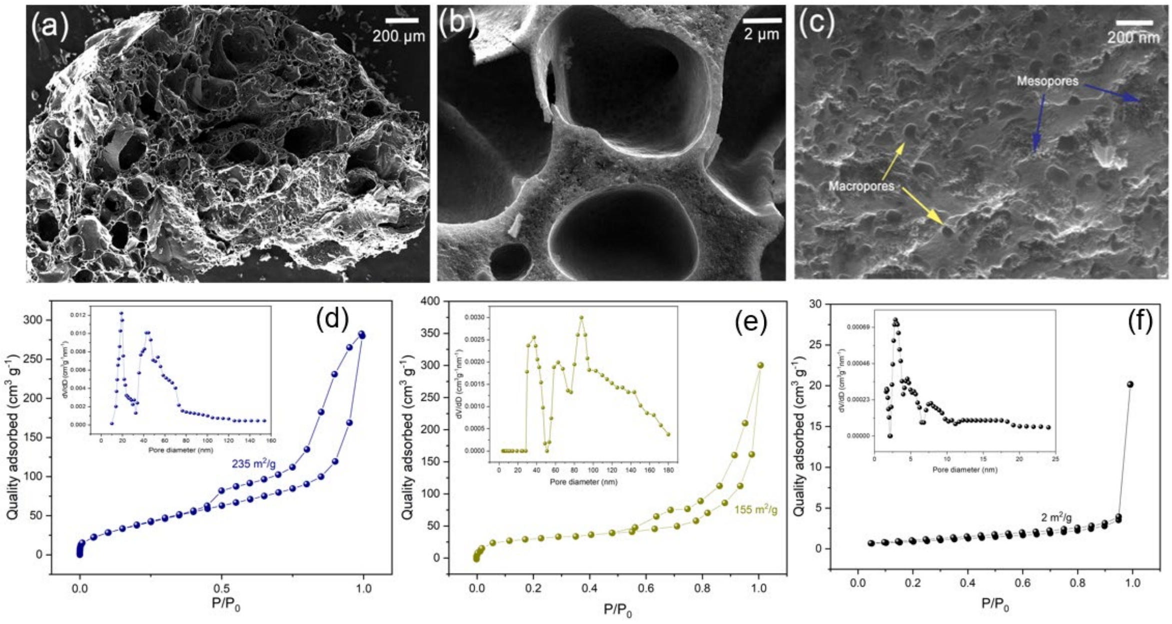

Figure 12. (a-c) SEM images of NSCA-700 (a-b) Low resolution (c) high resolution (d) N_2 adsorption-desorption isotherms of the NCA-700, CA-700, and commercial graphite, inside is the pore size distribution from DFT calculation.

The geometric surface area was probed by N_2 physisorption on the fabricated NCA-700, CA-700, and graphite (Figure 12 d-f). The typical hysteresis loop between the corresponding pressure (P/P_o) revealed a significant amount of the macro and meso pores in the aerogels, which served as the extended inner surface area. The NCA-700 possessed a relatively large specific surface area (SSA) (235 m^2/g) than the CA-700 (155 m^2/g) and commercial graphite (2 m^2/g), estimated by BET calculation. Moreover, the pore size distribution was determined by the DFT model. Two peaks located at 19 nm and 42 nm were exhibited in accordance with the widely distributed mesopores with a range of sizes.

Nevertheless, the CA-700 presented more macro-pores than the NCA-700. The lower surface area, as well as more extensive size pore distribution, were mainly attributed to the poor polymerization during the hydrolysis process and a large proportion of the ice sublimation during the freeze-drying process.[61] It could be referred that the N dopant could efficiently avoid the macromolecules aggregation and conductive to construct a larger accessible surface area, which facilitated the gas desorption process.

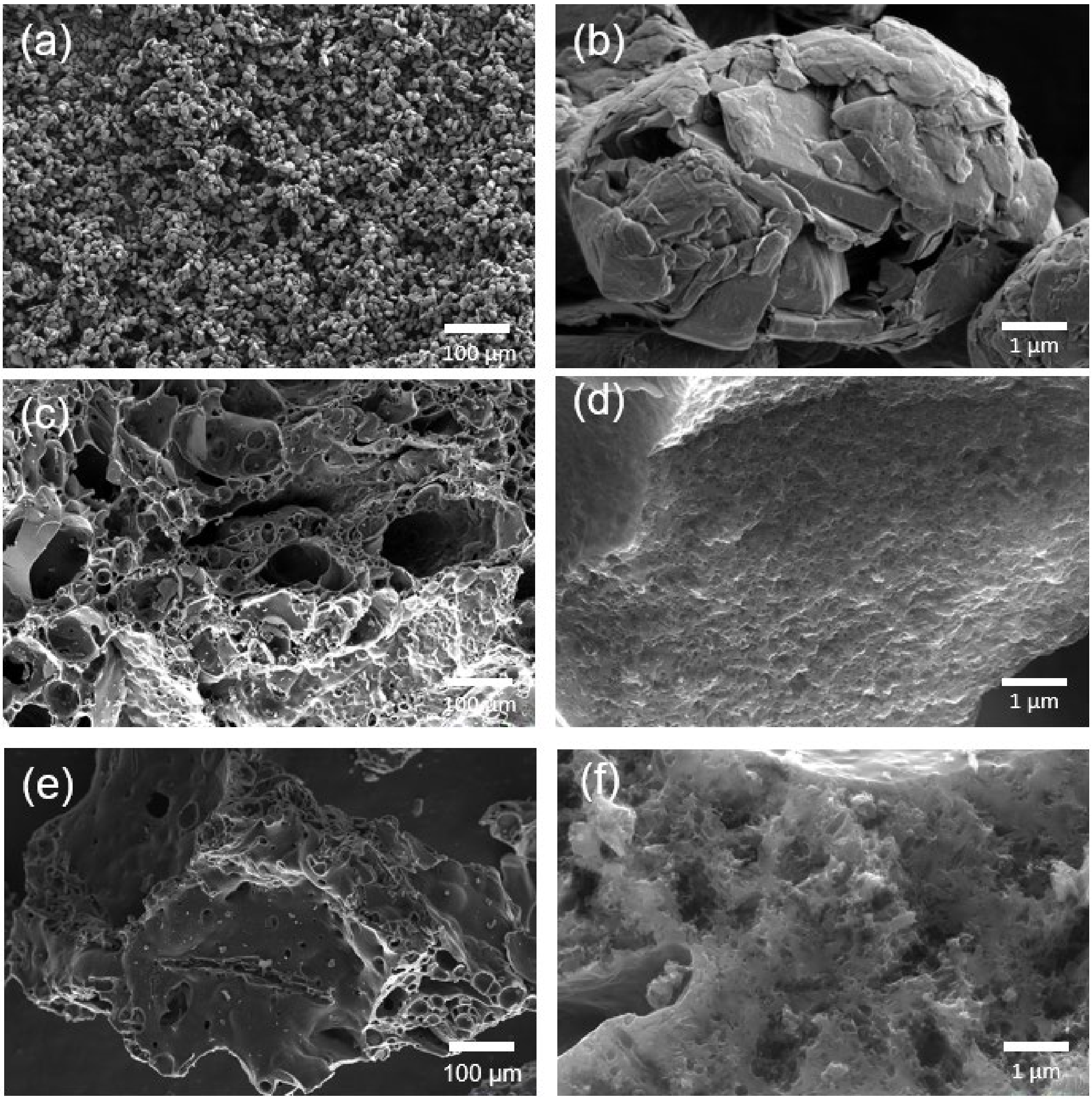

Figure S1. (a-b) SEM images of commercial natural graphite. (c-d) SEM images of NSCA-700. (e-f) SEM images of SCA-700.

The XPS measurements were examined to investigate the chemical environment and binding status. As illustrated in Figure 13 (a), the peaks were assigned to C, O, S elements from the carrageenan precursors.[62] The N was successfully doped into the aerogel as an additional peak appears at ~ 400 eV. The intensive C peak with an increased calcinating temperature was observed in the spectra, suggesting a higher graphitization degree. The significant amount of removal of O atoms in the aerogel was observed in the component numerical data when elevated temperature above 700 °C. On the contrary, the N atom% achieved a vertex at 700 °C after removal of most O contained groups. It was worth mentioning that despite the there was a trade-off relationship between pyrolysis temperature and N atom%, the dopant concentration was still considerable, mainly benefiting from the in-situ hybridization process.[63]

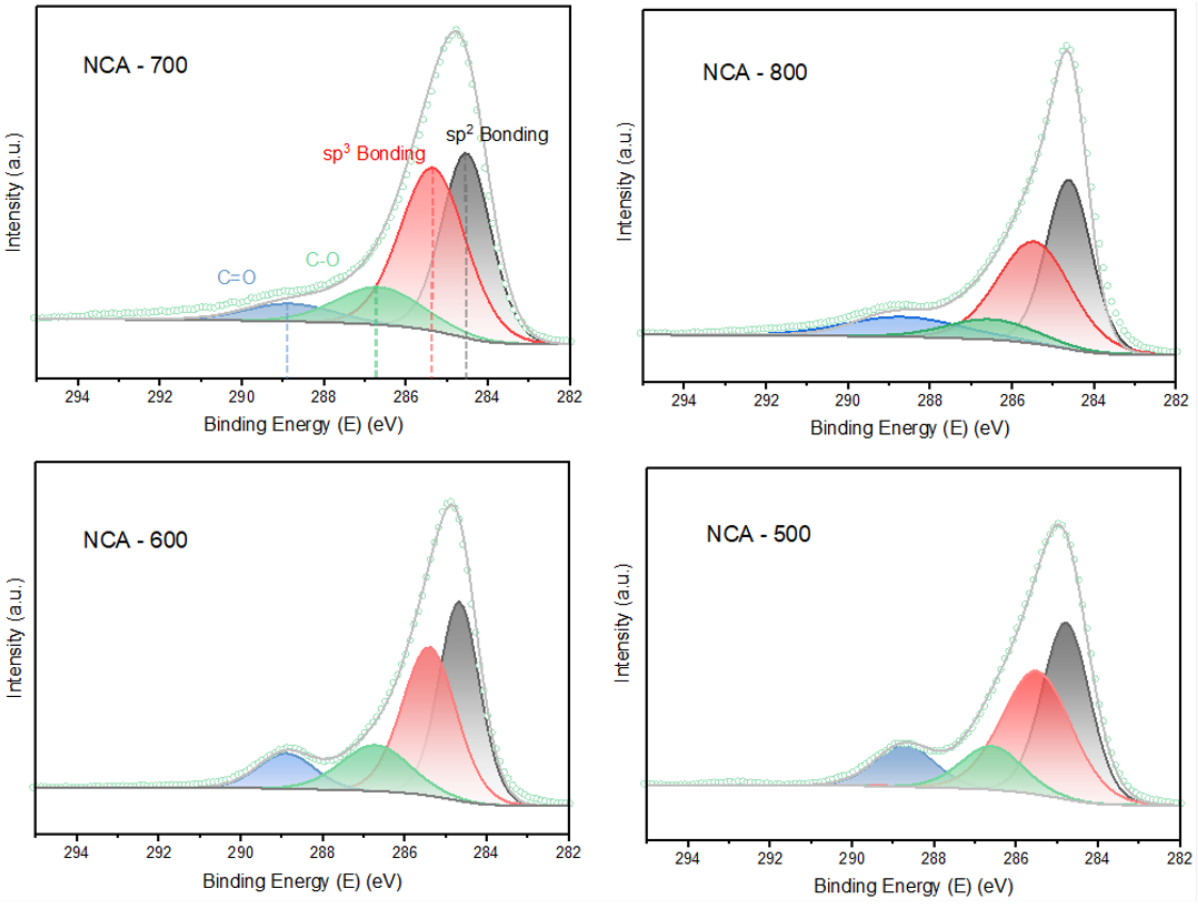

Figure S2. The deconvolution of C1s peak for high-resolution XPS spectra.

The C1s spectra could be deconvoluted into 4 characteristics peaks at 284.5 eV, 285.5 eV, 286.5 eV, 288.9 eV, which can be attributed to the sp^2 bonding, sp^3 bonding, C-O, and C=O (Figure S2).[64] The decreasing peak area of the C-O and C=O of the NCA-700 was ascribed to the lower concentration O atoms on the carbon matrix surface. Nevertheless, considering the inevitable physically absorbed oxygen on the porous aerogel structure, the content of the O groups is hard to be completely ruled out.[47]

The deconvolution of N1s presented 4 characteristic peaks, including pyridinic N (PDN) at 398.4 eV, pyrrolic N (PON) at 400.1 eV, graphitic N (GN) at 401 eV, and pyridinic oxide at 404 eV, respectively.[65] As Figure 13 (c) shown, the increasing GN atomic% from 500 °C to 700 °C leads to a destroy in graphitic sp^2 structure, hence breaking down the inert carbon neutrality and enables a high electroactivity for the chloride adsorption. Then, the Raman spectrum was employed to detect the disorder level (I_D/I_G ratio) in the carbon aerogels to gain further insight. As presented in Figure 13 (d), there are two intensive broad peaks located at 1345 and 1590 cm^{-1}, generated by the disordered carbon D band peak and crystalline graphitic G band peak.[66] For the as-fabricated carbon aerogels, the increasing I_D/I_G values were investigated with higher annealing temperatures. Surprisingly, a considerable increment was observed when elevated the temperature from 600 °C to 700 °C, which indicates some severe destroy occurred on the carbon matrix during this step change.

From a comparison of the XPS and Raman result in Figure 13 (c), the disordered level was highly relevant to the N atom%.[67] However, when keeping increasing the temperature over 700 °C, the partial removal of the GN% results in single vacancy generation as a schematic illustration in Figure 13 (e). Then, the atomic rearrangement and defects recombination occurred to accommodate the structural instability. This process could gently recover the carbon lattice, which leads to a smaller sp^2/sp^3 ratio. The specifical investigation of the topological defect was depicted in a published report in 2020.[65]

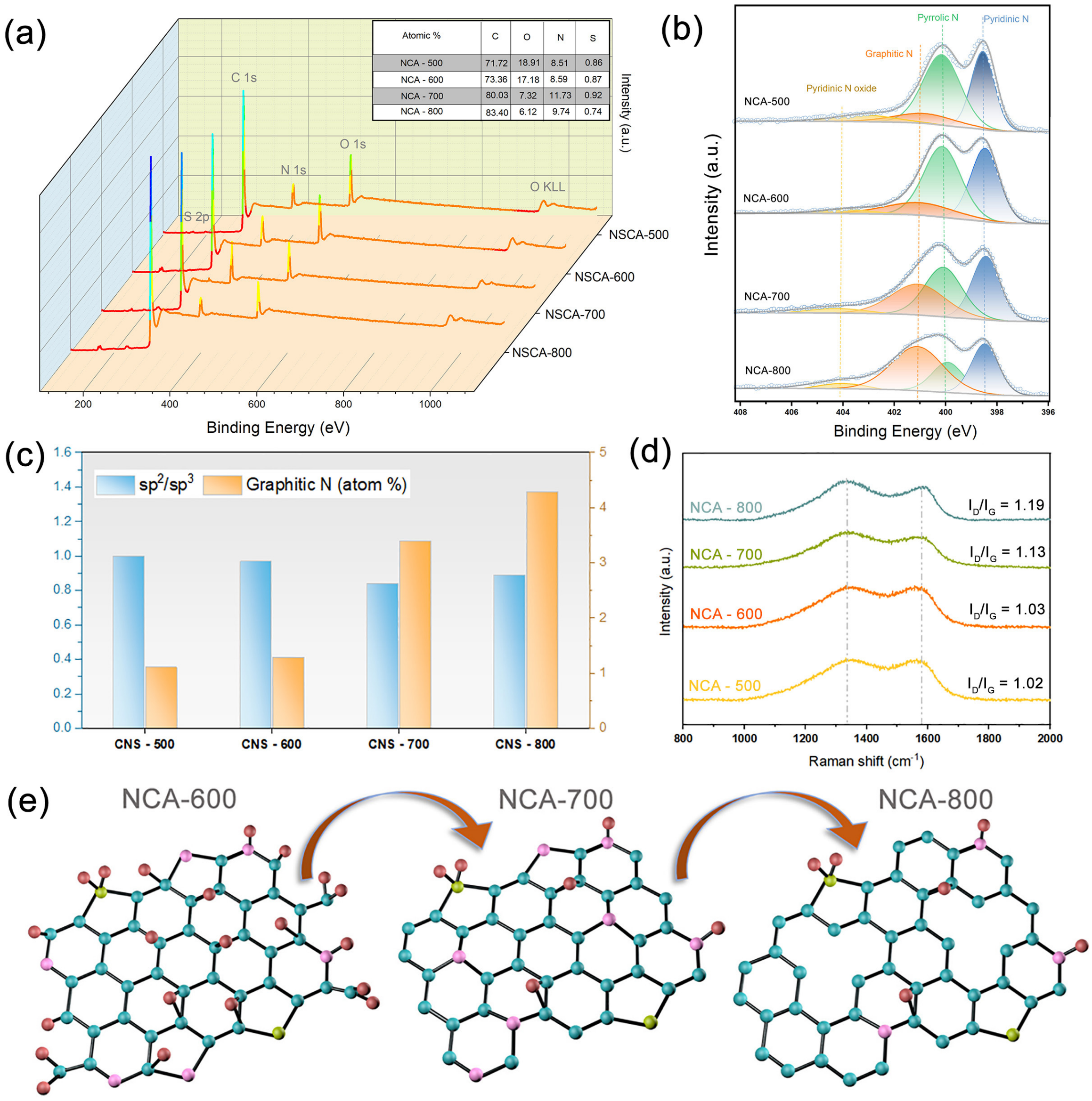

Figure 13. (a) XPS spectra of NCA with different annealing temperatures. (b) The high resolution of the N1s. (c) Comparison of the sp^2/sp^3 ratio and the graphitic N atom % among the different calcinating temperatures. (d) Comparison of the Raman spectra among the different calcinating temperatures. (e) Scheme of the transformation of the NCA from 600 °C to 800 °C.

The CER electrochemical performance was assessed using LSV polarization curves in concentrated Cl^-, acidic electrolyte at an applied potential between 1.2 V – 1.8 V *vs.* RHE. The standard equilibrium potential derived from the Nernst equation is 1.38 V vs. RHE under 25 ^{o}C and continuously Ar purging.[68] As shown in Figure 14 (a), all the calcinated N-doped aerogel possess well activity, among which the NCA-700 exhibited superior activity with only 295 mV overpotential to generate 10 mA cm^{-2}. As the first metal-free materials used for industrial electrode fabrication, the graphite is examined for performance comparison.[10] The CER activity of the graphite shown in Figure 14 (b) exhibited inferior performance with over 420 mV to generate less than 10 mA cm^{-2}. The pure carbon cloth exhibited negligible performance, suggesting the substrate has neglect contribution on the current generation in examining potential windows.

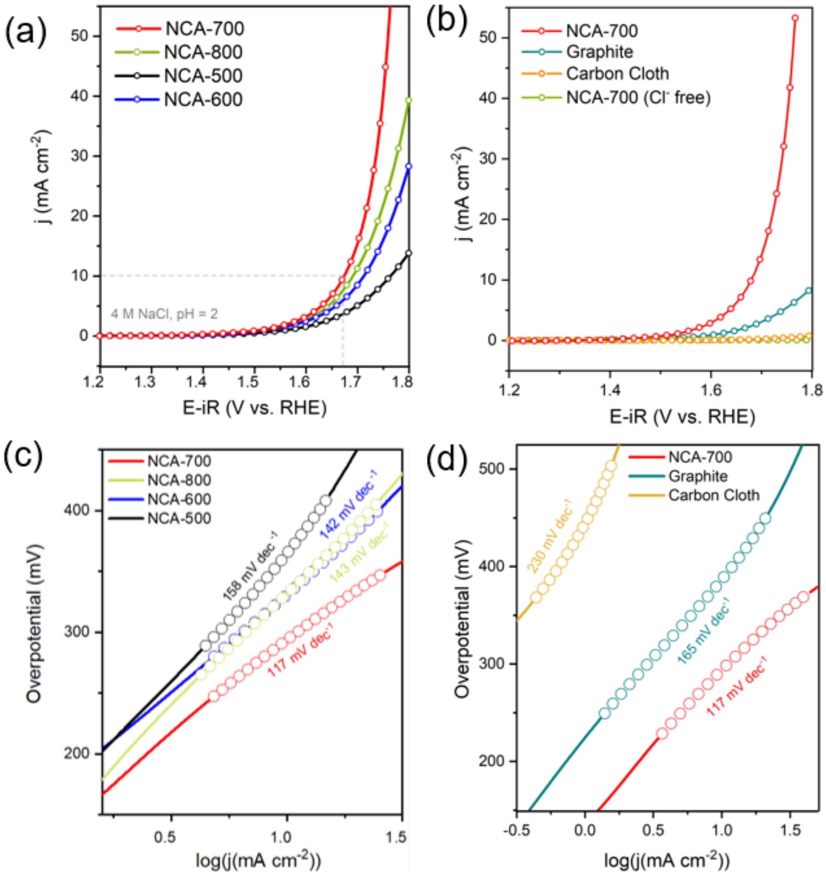

Figure 14. (a and c) LSV polarization curves and Tafel plots of NCA-500, NCA-600, NCA-700, NCA-800. (b and d) LSV polarization curves and Tafel plots of Graphite, carbon cloth. The polarization curve of NCA-700 in Cl^{-} absent environment is also shown, testing in 4 M NaClO$_4$, pH = 2 electrolyte.

The intrinsic catalytic activity was determined by evaluating Tafel plots (Figure 14 c and d). The Tafel plots of NCA-700 was 117 mV dec^{-2}, whereas those of the NCA-800, NCA-600, NCA-500, graphite, were 143 mV dec^{-2}, 142 mV dec^{-2}, 158 mV dec^{-2}, 165 mV dec^{-2} at the range of 250 mV - 450 mV, respectively. The lower Tafel slop revealed the fast kinetics of the NCA-700 than the other calcinating aerogels under different temperatures, and the heteroatoms doping could enable the better kinetic properties of the pure carbon materials.

The CER performances of the NCA-X were compared with the previously reported noble metal-free electrocatalysts, as presented in Figure 15. The metal-free NCA-700 exhibits a substantially lower overpotential to generate a 10 mA cm^{-2} than the most transition metal-based oxides. The superior activity as well as the lower price, suggests its promising potential to be applicable in the chlor-alkali process.

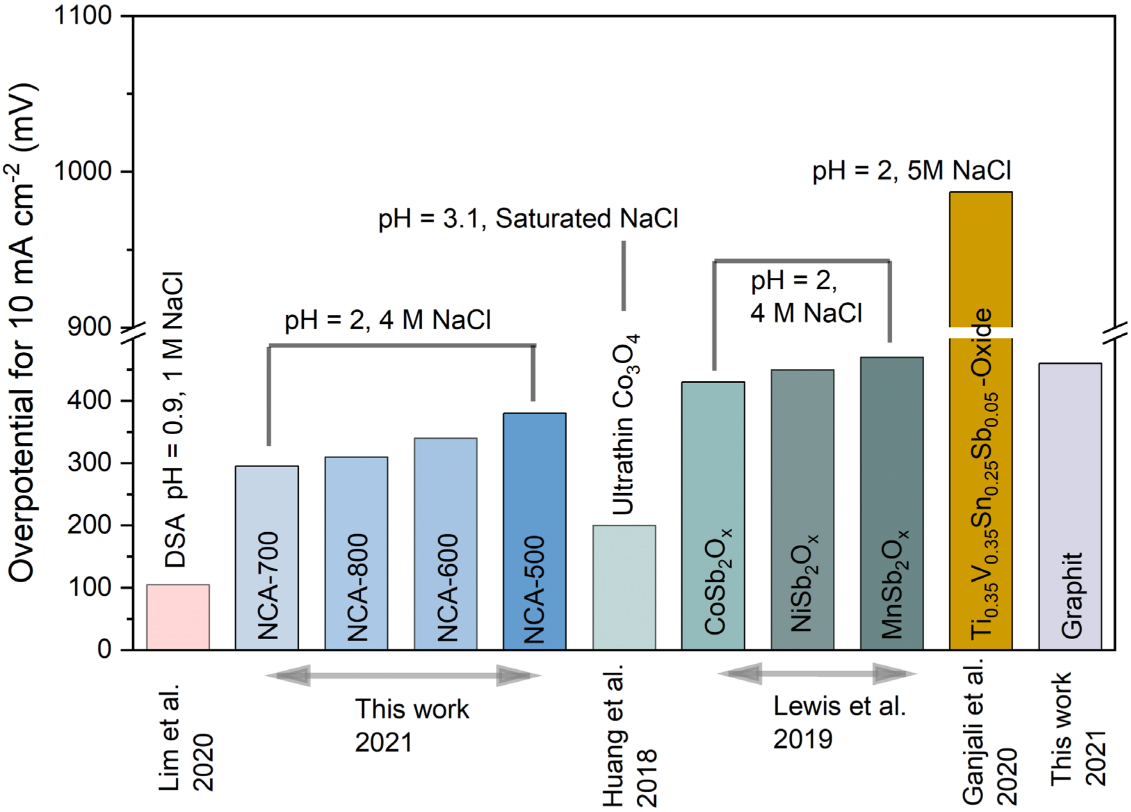

Figure 15. Comparison of the reported noble metal-free CER electrocatalysts' performance at an overpotential in 10 mA cm^{-2} current density.

The electrochemical double-layer capacitance was determined through scanning the CV in different scan rates as Figure 16 shown. Then, the ECSA of the NCA-X catalytic surface were calculated by dividing the Cs = 0.06 mF cm^{-2}. The resulted NCA-700 possessed a large ECSA with 250 cm^{-2} than the NCA-800, NCA-600, NCA-500 with 224 cm^2, 209 cm^2, 168 cm^2, respectively. It is noteworthy that we used the typical Cs value in a standard reported range of the acidic electrolyte. However, as the compressed and dispersed catalytic powders, there are errors in the accuracy when takes the microroughness, surface heterogeneity, and dispersion perfectness into the consideration. [69] Herein, we assumed that all the catalytic surface is extremely smooth with equally distributed active sites to better compare the active surface area of the calcinating aerogels under different temperatures.

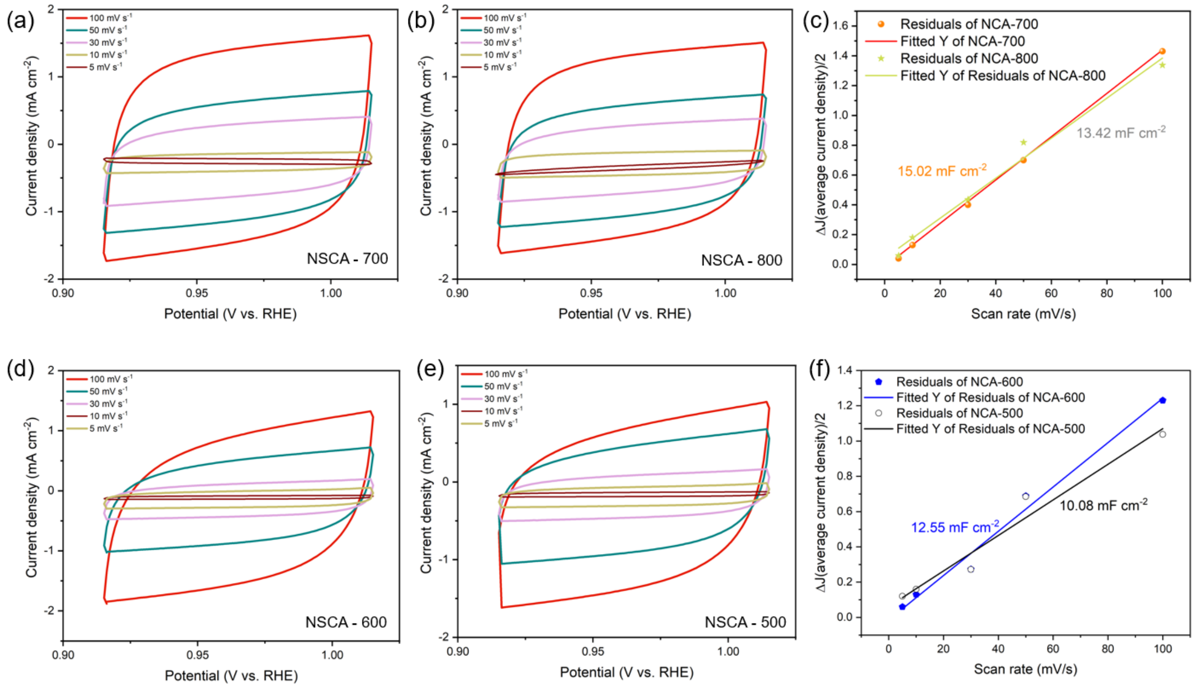

Figure 16. Successive increment of CV scan rates over the potential within 0.92 – 1.02 V vs. RHE and the linear relationship between difference of middle point of current density vs different scan rates. (a) NCA–700 (b) NCA–800 (d) NCA–600 (e) NCA–500 (c) NCA-700 and NCA-800 double layer capacitance measurement. (f) NCA-600 and NCA-500 double layer capacitance measurement.

Table 1. Faradaic efficiency estimation at a constant current density in a 5 min, 10 min, 30 min time intervals. All the electrode surface area are controlled at 1 cm^{-2}. Each NCA-X was tested for three time and the average applied potentials, experimental Cl_2 generations and faradaic efficiencies were presented as following.

N doped carbon aerogel	Potential (V) at 10 mA cm^{-2}	Cl_2 generation expected (μmol)	Cl_2 generation experimental (μmol)	Faradaic Efficiency (%)
Galvanostatic operation at constant 10 mA cm^{-2} current densities for 5 min				
NCA-500	1.778 ± 0.037	15.55	14.59 ± 0.36	93.8 ± 2.3
NCA-600	1.721 ± 0.028	15.55	14.69 ± 0.93	94.4 ± 5.3
NCA-700	1.675 ± 0.019	15.55	14.98 ± 0.59	96.3 ± 3.8
NCA-800	1.691 ± 0.027	15.55	14.77 ± 0.92	95.0 ± 5.9
Galvanostatic operation at constant 10 mA cm^{-2} current densities for 10 min				
NCA-500	1.778 ± 0.042	31.09	27.60 ± 0.48	88.8 ± 1.5
NCA-600	1.721 ± 0.036	31.09	28.13 ± 0.63	90.5 ± 2.0
NCA-700	1.675 ± 0.031	31.09	30.00 ± 1.08	96.5 ± 3.5
NCA-800	1.691 ± 0.026	31.09	30.19 ± 1.04	97.1 ± 3.3
Galvanostatic operation at constant 10 mA cm^{-2} current densities for 30 min				
NCA-500	1.778 ± 0.036	93.28	80.62 ± 2.25	83.5 ± 2.8
NCA-600	1.721 ± 0.048	93.28	79.17 ± 3.82	84.9 ± 4.1
NCA-700	1.675 ± 0.018	93.28	97.92 ± 0.72	94.3 ± 0.8
NCA-800	1.691 ± 0.026	93.28	84.46 ± 2.96	92.7 ± 3.2

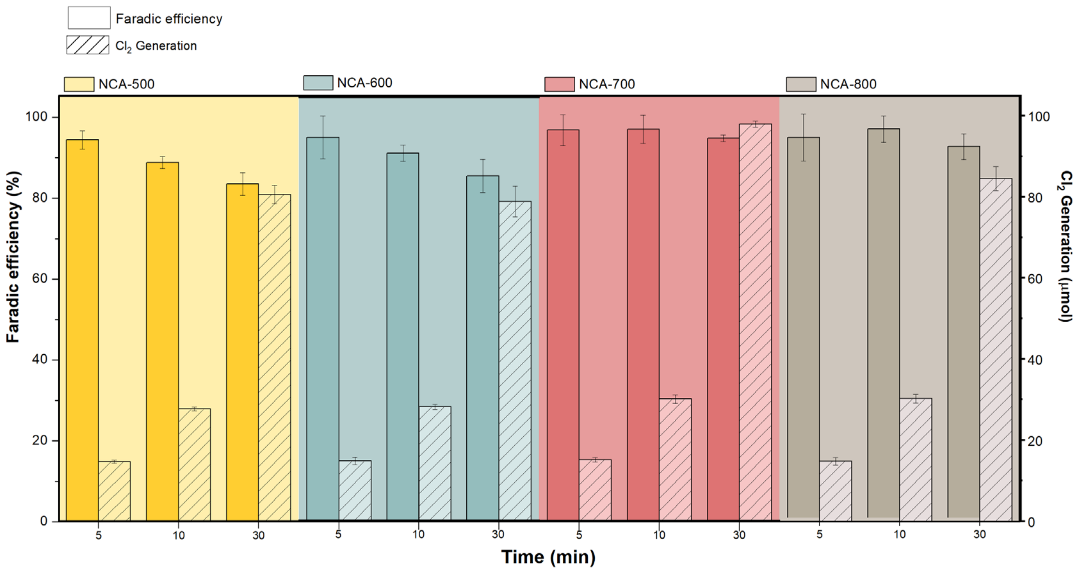

Figure 17. Faradaic efficiencies and Cl_2 generation of the NCA-X were determined at a constant current density in 5 min, 10 min, 30 min time intervals.

Another critical parameter to evaluate the CER performance is the faradaic efficiency, which mainly respects to the Cl_2 production efficiency during the electrolysis. As the competitive OER occurring, the selectivity toward Cl_2 could be variant with electrolyte conditions, operating conditions, and reaction time.[1] Herein, we control the electrolyte and operating conditions during the measurement, examining the faradaic efficiency of the NCA-X changes over time. As Table 1 and Figure 17 shown, the calcinating at a 700 °C and 800 °C presented better selectivity toward Cl_2 than the others. When prolonging the reaction time to 30 min, both NCA-500 and NCA-600 appeared to attenuate faradaic efficiencies. Referring to the previous research on OER, the lower current efficiencies may be attributed to the more oxygen-containing groups of the carbon substrate of NCA-500 and NCA-600, which enable electrocatalytic oxygen production. [70] While removing partial oxygen functionalized groups, the faradaic efficiencies could be maintained well as NCA-700 and NCA-800 exhibited. However, the current exploration on the selectivity study of carbon materials is insufficient to gain a deep insight, and the real mechanism should be augmented by more in-depth study.

The charge transfer resistance (R_{ct}) of the NCA-X was revealed in Nyquist plots, in which the smaller diameter of the semicircle represents the less resistance between electrolyte and electrocatalyst surface. As Figure 18 (a) shown, the fabricated NCA-700 exhibited the smallest R_{ct}, possessing the highest conductivity, which is crucial for generating a promising catalytic activity in CER. A similar result that the N-doped CNT substrate pyrolyzed at 700 °C exhibits lower R_{ct} and superior performance toward CER, was also reported in Lim et al.'s work.[29,45] A reduction in R_{ct} was observed when elevating the temperature from 500 °C to 700 °C. This should be attributed to the two factors, one is the increasing graphitization level, the other is more N atom% in the carbon matrix. However, corresponding to the XPS and Raman results, overheating to the 800 °C results in the dopant removal and more defects generation, hence inferior conductivity.

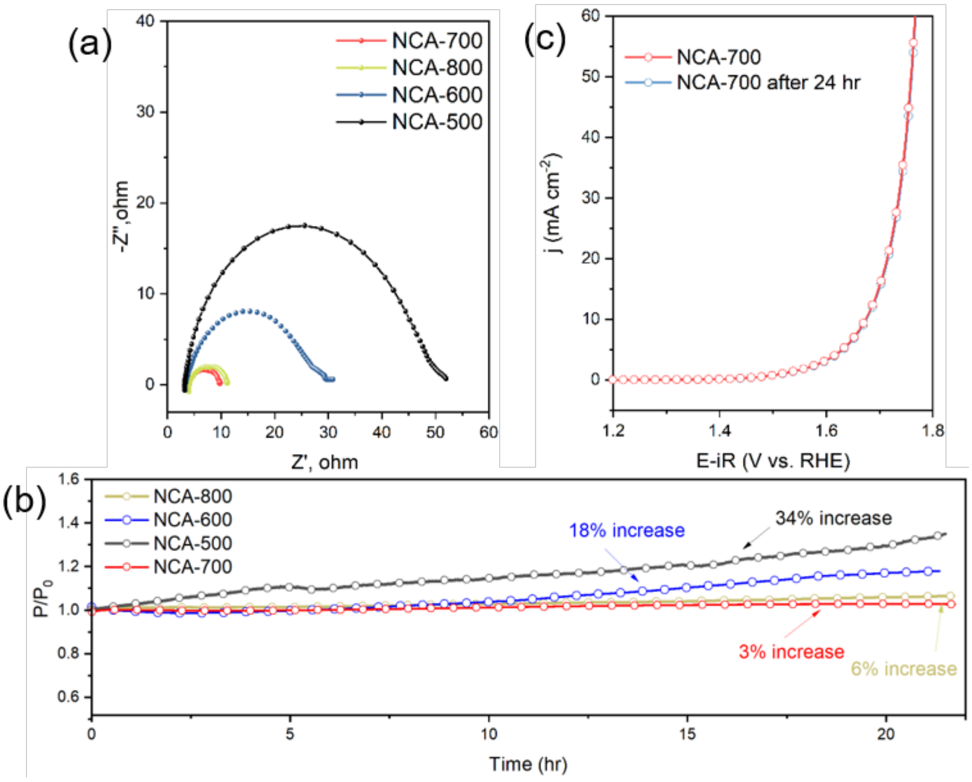

Figure 18. (a) Nyquist plots of NCA-X at a constant overpotential of 295 mV. (b) Polarization curves before and after stability testing. (c) Chronoamperometry of NCA-X testings for 24 hrs.

Moreover, the long-term stability was determined by holding a constant current density for 24 hrs, while the applied potentials were kept recording as a function of time. NCA-700 exhibited outstanding stability with merely a 3% potential rise to maintain a constant current density and there is neglectable activity reduction after 24 hours, as Figure 18 b shown. As a comparison, both NCA-500 and NCA-600 required 18% and 34% more potential, which represents their deactivation behavior during the long-term process. This result is possibly attributed to the increasing GN in the NCA-700, which acts as the stable active sites to sustain a high performance in acidic electrolyte, as Figure 18 (c).[71]

Chapter 5. Conclusion and Outlook

Conclusion

In this work, we have successfully developed a carbon-based metal-free electrocatalyst through a low-cost, scalable approach. The biomass-derived carbon aerogel doped with N exhibits excellent performance toward CER under a 700 ºC calcinating temperature, with an overpotential of 295 mV to deliver 10 mV cm^{-2} current density and a Tafel slope of 117 mV dec^{-1}, which is comparable or even superior to the transition metal-based electrocatalyst reported so far. The as-synthesized NCA-700 also demonstrates high selectivity (~95%) for 30 min and well stability with merely 3% loss. The result suggests that the carbon-based metal-free electrocatalyst could be modified to become a potential cost-effective CER electrocatalyst, which holds great promise in the future chlor-alkali process development.

Outlook

Despite significant progress has been made on the electrocatalytic Cl_2 production, the current explored novel electrocatalysts and mechanisms behind are still insufficient and intensive effort in the following aspects is expected in the future.

Catalyst design

For a half-century, the research on developing the highly efficient CER electrocatalyst still remains on mixing with the multi-metal oxides, attempting to reduce the precious metal utilization while maintaining the satisfying catalytic ability. However, the inevitable selectivity issue, substrate passivation problem, and high cost significantly limit further development. Recently, the atomically dispersed Pt sites on CNT have exhibited exceptional activity as well as selectivity toward CER, which reveals the carbon materials could serve as the promising substrate to eliminate the competition to the OER in the neutral or low Cl^- concentration electrolyte. In fact, the single-atom catalysts (SAC), owing to their high atom utilization efficiency, controllable metal—substrate design, and distinctive quantum size effects, have attracted tremendous attention in the various electrocatalytic process.[72–75] More research on employing the novel SAC is anticipated to deeply explore the quantum atomic effect of the Cl^- oxidation process.

Apart from the metal-based electrocatalysts, the metal-free electrocatalysts hold great promise in attracting worldwide attention again, as the graphite once did. This research reported that more heteroatom-doped carbon materials are expected to explore the different doping-induced charge redistribution in the electroneutrality carbon matrix. By extension, the co-doping of the various heteroatoms species is also a promising strategy to pursue the potential synergetic effect.

Mechanism study

Despite the CER mechanism process on the RuO_2 has been explained through thermodynamic and kinetic study, the fundamental research on the carbon materials has rarely been mentioned. It is significant to figure out the real active catalytic active sites in the carbon-based materials so that the more efficiently metal-free catalysts could be well designed. To this end, more theoretical studies and computational models are well expected to explore carbon materials deeply. Also, the research on identifying the intermediate formation of the carbon materials during the CER is anticipated with employing advanced characterization techniques, such as *in-situ* X ray absorption spectrum (XAS) and *in-situ* FTIR and Raman spectroscopy.[3] The successful incorporation of the theoretical mechanism and the modern characterization techniques could effectively guide the novel metal-free catalyst design in the future.

Reference

1. Karlsson, R. K. B. & Cornell, A. Selectivity between Oxygen and Chlorine Evolution in the Chlor-Alkali and Chlorate Processes. *Chem. Rev.* **116**, 2982–3028 (2016).

2. A. sector group of Cefic. *Chlor-Alkali Review 2019-2020.* https://www.chlorineindustryreview.com/wp-content/uploads/2020/09/Industry-Review-2019_2020.pdf (2020).

3. Wang, Y., Liu, Y., Wiley, D., Zhao, S. & Tang, Z. Recent advances in electrocatalytic chloride oxidation for chlorine gas production. *J. Mater. Chem. A* **9**, 18974–18993 (2021).

4. Moussallem, I., Jörissen, J., Kunz, U., Pinnow, S. & Turek, T. Chlor-alkali electrolysis with oxygen depolarized cathodes: History, present status and future prospects. *J. Appl. Electrochem.* **38**, 1177–1194 (2008).

5. Li, K. *et al.* Revisiting Chlor-Alkali Electrolyzers: from Materials to Devices. *Trans. Tianjin Univ.* **27**, 202–216 (2021).

6. Mosa, A. & Duffin, J. The interwoven history of mercury poisoning in Ontario and Japan. *CMAJ* **189**, E213–E215 (2017).

7. Garcia-Herrero, I., Margallo, M., Onandía, R., Aldaco, R. & Irabien, A. Environmental challenges of the chlor-alkali production: Seeking answers from a life cycle approach. *Sci. Total Environ.* **580**, 147–157 (2017).

8. Lindley, A. A. An economic and environmental analysis of the chlor-alkali production process. **511385**, (1997).

9. Otashu, J. I. & Baldea, M. Demand response-oriented dynamic modeling and operational optimization of membrane-based chlor-alkali plants. *Comput. Chem. Eng.*

121, 396–408 (2019).

10. Janssen, L. J. J. & Hoogland, J. G. Electrolysis of acidic NaCl solution with a graphite anode-I. The graphite electrode. *Electrochim. Acta* **14**, 1097–1108 (1969).

11. Beer, H. B. *Method of making an electrode having a coating comprising a platinum metal, oxide*. (1974).

12. Arikado, T., Iwakura, C. & Tamura, H. Chlorine evolution reaction on platinum and several alloys. *Electrochim. Acta* **22**, 229–232 (1977).

13. Beer, H. B. The Invention and Industrial Development of Metal Anodes. *J. Electrochem. Soc.* **127**, 303C-307C (1980).

14. Trasatti, S. Electrocatalysis: Understanding the success of DSA®. *Electrochim. Acta* **45**, 2377–2385 (2000).

15. Burrows, I. R., Denton, D. A. & Harrison, J. A. Chlorine and oxygen evolution on various compositions of RuO2/TiO2 electrodes. *Electrochim. Acta* **23**, 493–500 (1978).

16. Over, H. Surface Chemistry of Ruthenium Dioxide in Heterogeneous Catalysis and Electrocatalysis: From Fundamental to Applied Research. *Chem. Rev.* **112**, 3356–3426 (2012).

17. Comninellis, C. & Vercesi, G. P. Characterization of DSA-Type electrodes : choice of a coating. *J. Appl. Electrochem.* **21**, 335–345 (1991).

18. Chen, R. *et al.* Anodic electrocatalytic coatings for electrolytic chlorine production: A review. *Zeitschrift fur Phys. Chemie* **227**, 651–666 (2013).

19. Exner, K. S., Anton, J., Jacob, T. & Over, H. Controlling Selectivity in the Chlorine

Evolution Reaction over RuO 2 -Based Catalysts . *Angew. Chemie* **126**, 11212–11215 (2014).

20. Exner, K. S. Controlling Stability and Selectivity in the Competing Chlorine and Oxygen Evolution Reaction over Transition Metal Oxide Electrodes. *ChemElectroChem* **6**, 3401–3409 (2019).

21. Bommaraju, T. V, Chen, C. P. & Birss, V. I. Deactivation of thermally formed RuO2+ TiO2 coatings during chlorine evolution: Mechanisms and reactivation measures. *Mod. Chlor-Alkali Technol.* **8**, 57 (2001).

22. Niksa, M. J. & Rudd, E. J. Precious metal containing mixed metal oxide (MMO) electrodes By Water Star Inc. *Water Star* 1–8.

23. Trasatti, S. Progress in the understanding of the mechanism of chlorine evolution at oxide electrodes. *Electrochimica Acta* vol. 32 369–382 (1987).

24. Hansen, H. A. *et al.* Electrochemical chlorine evolution at rutile oxide (110) surfaces. *Phys. Chem. Chem. Phys.* **12**, 283–290 (2010).

25. Exner, K. S., Anton, J., Jacob, T. & Over, H. Angewandte Controlling Selectivity in the Chlorine Evolution Reaction over RuO 2 - Based Catalysts **. **201406112**, 11212–11215 (2014).

26. Exner, K. S., Anton, J., Jacob, T. & Over, H. Chlorine Evolution Reaction on RuO2(110): Ab initio Atomistic Thermodynamics Study - Pourbaix Diagrams. *Electrochim. Acta* **120**, 460–466 (2014).

27. Exner, K. S., Anton, J., Jacob, T. & Over, H. Microscopic Insights into the Chlorine Evolution Reaction on RuO2(110): a Mechanistic Ab Initio Atomistic Thermodynamics Study. *Electrocatalysis* **6**, 163–172 (2015).

28. Exner, K. S. Design criteria for the competing chlorine and oxygen evolution reactions: avoid the OCl adsorbate to enhance chlorine selectivity. *Phys. Chem. Chem. Phys.* **22**, 22451–22458 (2020).

29. Lim, T. *et al.* General Efficacy of Atomically Dispersed Pt Catalysts for the Chlorine Evolution Reaction: Potential-Dependent Switching of the Kinetics and Mechanism. *ACS Catal.* **11**, 12232–12246 (2021).

30. Exner, K. S. Beyond Dimensionally Stable Anodes: Single-Atom Catalysts with Superior Chlorine Selectivity. *ChemElectroChem* **7**, 1528–1530 (2020).

31. Zeradjanin, A. R., Menzel, N., Schuhmann, W. & Strasser, P. On the faradaic selectivity and the role of surface inhomogeneity during the chlorine evolution reaction on ternary Ti-Ru-Ir mixed metal oxide electrocatalysts. *Phys. Chem. Chem. Phys.* **16**, 13741–13747 (2014).

32. Xiong, K. *et al.* Sn and Sb co-doped RuTi oxides supported on TiO2 nanotubes anode for selectivity toward electrocatalytic chlorine evolution. *J. Appl. Electrochem.* **43**, 847–854 (2013).

33. Kötz, R. & Stucki, S. Stabilization of RuO2 by IrO2 for anodic oxygen evolution in acid media. *Electrochim. Acta* **31**, 1311–1316 (1986).

34. Xiong, K. *et al.* In situ growth of RuO2–TiO2 catalyst with flower-like morphologies on the Ti substrate as a binder-free integrated anode for chlorine evolution. *J. Appl. Electrochem.* **46**, 841–849 (2016).

35. Menzel, N., Ortel, E., Mette, K., Kraehnert, R. & Strasser, P. Dimensionally stable Ru/Ir/TiO2-anodes with tailored mesoporosity for efficient electrochemical chlorine evolution. *ACS Catal.* **3**, 1324–1333 (2013).

36. Chen, X., Chen, G. & Yue, P. L. Stable Ti/IrOx−Sb2O5−SnO2 Anode for O2 Evolution with Low Ir Content. *J. Phys. Chem. B* **105**, 4623–4628 (2001).

37. Wang, S., Xu, H., Yao, P. & Chen, X. Ti/RuO 2-IrO 2-SnO 2-Sb 2 O 5 Anodes for Cl 2 Evolution from Seawater. *Artic. Electrochem.* **80**, 507–511 (2012).

38. Xiong, K. *et al.* Sn and Sb co-doped RuTi oxides supported on TiO2 nanotubes anode for selectivity toward electrocatalytic chlorine evolution. *J. Appl. Electrochem.* **43**, 847–854 (2013).

39. Panić, V. V., Dekanski, A., Milonjić, S. K., Atanasoski, R. T. & Nikolić, B. Ž. RuO2-TiO2 coated titanium anodes obtained by the sol-gel procedure and their electrochemical behaviour in the chlorine evolution reaction. *Colloids Surfaces A Physicochem. Eng. Asp.* **157**, 269–274 (1999).

40. Goudarzi, M. & Ghorbani, M. A study on ternary mixed oxide coatings containing Ti, Ru, Ir by sol–gel method on titanium. *J. Sol-Gel Sci. Technol.* **73**, 332–340 (2014).

41. Chen, R. *et al.* Microstructural impact of anodic coatings on the electrochemical chlorine evolution reaction. *Phys. Chem. Chem. Phys.* **14**, 7392–7399 (2012).

42. Mirzaei, M. *et al.* A selective and efficient precious metal-free electrocatalyst for chlorine evolution reaction: An experimental and computational study. *Chem. Eng. J.* 127785 (2020) doi:10.1016/j.cej.2020.127785.

43. Zhu, X. *et al.* Co3O4 nanobelt arrays assembled with ultrathin nanosheets as highly efficient and stable electrocatalysts for the chlorine evolution reaction. *J. Mater. Chem. A* **6**, 12718–12723 (2018).

44. Moreno-Hernandez, I. A., Brunschwig, B. S. & Lewis, N. S. Crystalline nickel, cobalt, and manganese antimonates as electrocatalysts for the chlorine evolution reaction.

Energy Environ. Sci. **12**, 1241–1248 (2019).

45. Lim, T. *et al.* Atomically dispersed Pt–N4 sites as efficient and selective electrocatalysts for the chlorine evolution reaction. *Nat. Commun.* **11**, (2020).

46. Zhao, S., Wang, D.-W., Amal, R. & Dai, L. Carbon-Based Metal-Free Catalysts for Key Reactions Involved in Energy Conversion and Storage. *Adv. Mater.* **31**, 1801526 (2019).

47. Zhang, J., Zhao, Z., Xia, Z. & Dai, L. A metal-free bifunctional electrocatalyst for oxygen reduction and oxygen evolution reactions. *Nat. Nanotechnol.* **10**, 444–452 (2015).

48. Zhao, S., Lu, X., Wang, L., Gale, J. & Amal, R. Carbon-Based Metal-Free Catalysts for Electrocatalytic Reduction of Nitrogen for Synthesis of Ammonia at Ambient Conditions. *Adv. Mater.* **31**, 1–9 (2019).

49. Jia, Y. *et al.* Defect Graphene as a Trifunctional Catalyst for Electrochemical Reactions. 9532–9538 (2016) doi:10.1002/adma.201602912.

50. Chi, M. *et al.* Lignin-based monolithic carbon electrode decorating with RuO2 nanospheres for high-performance chlorine evolution reaction. *Ind. Crops Prod.* **159**, 113088 (2021).

51. Hu, C., Paul, R., Dai, Q. & Dai, L. Carbon-based metal-free electrocatalysts: from oxygen reduction to multifunctional electrocatalysis. *Chem. Soc. Rev.* (2021) doi:10.1039/D1CS00219H.

52. Paul, R., Dai, Q., Hu, C. & Dai, L. Ten years of carbon-based metal-free electrocatalysts. *Carbon Energy* **1**, 19–31 (2019).

53. Li, D. *et al.* A Defect-Driven Metal-free Electrocatalyst for Oxygen Reduction in

Acidic Electrolyte. *Chem* **4**, 2345–2356 (2018).

54. Xiong, B., Chen, L. & Shi, J. Anion-Containing Noble-Metal-Free Bifunctional Electrocatalysts for Overall Water Splitting. *ACS Catal.* **8**, 3688–3707 (2018).

55. McCrory, C. C. L., Jung, S., Peters, J. C. & Jaramillo, T. F. Benchmarking heterogeneous electrocatalysts for the oxygen evolution reaction. *J. Am. Chem. Soc.* **135**, 16977–16987 (2013).

56. Vos, J. G. & Koper, M. T. M. Measurement of competition between oxygen evolution and chlorine evolution using rotating ring-disk electrode voltammetry. *J. Electroanal. Chem.* **819**, 260–268 (2018).

57. Dai, L., Xue, Y., Qu, L., Choi, H.-J. & Baek, J.-B. Metal-Free Catalysts for Oxygen Reduction Reaction. *Chem. Rev.* **115**, 4823–4892 (2015).

58. Kuanping, G., Feng, D., Zhenhai, X., Michael, D. & Liming, D. Nitrogen-Doped Carbon Nanotube Arrays with High Electrocatalytic Activity for Oxygen Reduction. *Science.* **323**, 760–764 (2009).

59. Doyle, J., Giannouli, P., Philp, K. & Morris, E. R. Effect of K+ and Ca2+ cations on gelation of κ-carrageenan. *Gums Stabilisers Food Ind. 11* **11**, 158–164 (2002).

60. Abecassis-Wolfovich, M. *et al.* Texture and nanostructure of chromia aerogels prepared by urea-assisted homogeneous precipitation and low-temperature supercritical drying. *J. Non. Cryst. Solids* **318**, 95–111 (2003).

61. Guastaferro, M., Reverchon, E. & Baldino, L. Polysaccharide-based aerogel production for biomedical applications: A comparative review. *Materials (Basel).* **14**, (2021).

62. Hettle, A. G. *et al.* Insights into the κ/ι-carrageenan metabolism pathway of some

marine Pseudoalteromonas species. *Commun. Biol.* **2**, (2019).

63. Pei, Z. *et al.* Texturing in situ: N,S-enriched hierarchically porous carbon as a highly active reversible oxygen electrocatalyst. *Energy Environ. Sci.* **10**, 742–749 (2017).

64. Dwivedi, N. *et al.* Understanding the role of nitrogen in plasma-assisted surface modification of magnetic recording media with and without ultrathin carbon overcoats. *Sci. Rep.* **5**, (2015).

65. Wang, X. *et al.* A Directional Synthesis for Topological Defect in Carbon. *Chem* **6**, 2009–2023 (2020).

66. Pei, Z. *et al.* Texturing in situ: N,S-enriched hierarchically porous carbon as a highly active reversible oxygen electrocatalyst. *Energy Environ. Sci.* **10**, 742–749 (2017).

67. Zhao, S. *et al.* Carbonized nanoscale metal-organic frameworks as high performance electrocatalyst for oxygen reduction reaction. *ACS Nano* **8**, 12660–12668 (2014).

68. Guerrini, E., Consonni, V. & Trasatti, S. Surface and electrocatalytic properties of well-defined and vicinal RuO 2 single crystal faces. *J. Solid State Electrochem.* **9**, 320–329 (2005).

69. Trasatti, S. & Petrii, O. A. International Union of Pure and Applied Chemistry Physical Chemistry Division Commission on Electrochemistry: Real Surface Area Measurements in Electrochemistry. *Pure Appl. Chem.* **63**, 711–734 (1991).

70. Lu, X., Yim, W. L., Suryanto, B. H. R. & Zhao, C. Electrocatalytic oxygen evolution at surface-oxidized multiwall carbon nanotubes. *J. Am. Chem. Soc.* **137**, 2901–2907 (2015).

71. Bhange, S. N., Unni, S. M. & Kurungot, S. Nitrogen and sulphur co-doped crumbled graphene for the oxygen reduction reaction with improved activity and stability in

acidic medium. *J. Mater. Chem. A* **4**, 6014–6020 (2016).

72. Yang, Y. *et al.* Recent Progress of Carbon-Supported Single-Atom Catalysts for Energy Conversion and Storage. *Matter* **3**, 1442–1476 (2020).

73. Zhu, C., Fu, S., Shi, Q., Du, D. & Lin, Y. Single-Atom Electrocatalysts. *Angew. Chemie - Int. Ed.* **56**, 13944–13960 (2017).

74. Wang, A., Li, J. & Zhang, T. Heterogeneous single-atom catalysis. *Nat. Rev. Chem.* **2**, 65–81 (2018).

75. Kim, J., Kim, H. E. & Lee, H. Single-Atom Catalysts of Precious Metals for Electrochemical Reactions. *ChemSusChem* **11**, 104–113 (2018).